1-1-2010

Effect of a Soluble Surfactant on a Finite-Sized Bubble Motion in a Blood Vessel

Tirumani N. Swaminathan
University of Pennsylvania, tnswamin@seas.upenn.edu

Karthik Mukundakrishnan
University of Pennsylvania, karthikm@seas.upenn.edu

Portonovo S. Ayyaswamy
University of Pennsylvania, ayya@seas.upenn.edu

David M. Eckmann
University of Pennsylvania, eckmanndm@uphs.upenn.edu

Suggested Citation:
Swaminathan, Tirumani, et. al. (2010) *Effect of a soluble surfactant on a finite-sized bubble motion in a blood vessel.* Journal of Fluid Mechanics. Vol. 642 , pp. 509–539.

Effect of a Soluble Surfactant on a Finite-Sized Bubble Motion in a Blood Vessel

Abstract
We present detailed results for the motion of a finite-sized gas bubble in a blood vessel. The bubble (dispersed phase) size is taken to be such as to nearly occlude the vessel. The bulk medium is treated as a shear thinning Casson fluid and contains a soluble surfactant that adsorbs and desorbs from the interface. Three different vessel sizes, corresponding to a small artery, a large arteriole, and a small arteriole, in normal humans, are considered. The haematocrit (volume fraction of RBCs) has been taken to be 0.45. For arteriolar flow, where relevant, the Fahraeus–Lindqvist effect is taken into account. Bubble motion causes temporal and spatial gradients of shear stress at the cell surface lining the vessel wall as the bubble approaches the cell, moves over it and passes it by. Rapid reversals occur in the sign of the shear stress imparted to the cell surface during this motion. Shear stress gradients together with sign reversals are associated with a recirculation vortex at the rear of the moving bubble. The presence of the surfactant reduces the level of the shear stress gradients imparted to the cell surface as compared to an equivalent surfactant-free system. Our numerical results for bubble shapes and wall shear stresses may help explain phenomena observed in experimental studies related to gas embolism, a significant problem in cardiac surgery and decompression sickness.

Keywords
blood vessel, embolism, finite-sized bubble motion, front tracking scheme, surfactant

Comments
Suggested Citation:
Swaminathan, Tirumani, et. al. (2010) *Effect of a soluble surfactant on a finite-sized bubble motion in a blood vessel.* Journal of Fluid Mechanics. Vol. 642 , pp. 509–539.

J. Fluid Mech. (2010), *vol.* 642, *pp.* 509–539.
doi:10.1017/S0022112009992692

Effect of a soluble surfactant on a finite-sized bubble motion in a blood vessel

T. N. SWAMINATHAN[1,2], K. MUKUNDAKRISHNAN[2], P. S. AYYASWAMY[2]† AND D. M. ECKMANN[1]

[1]Department of Anesthesiology and Critical Care, University of Pennsylvania, PA 19104, USA

[2]Department of Mechanical Engineering and Applied Mechanics, University of Pennsylvania, PA 19104, USA

(Received 26 May 2009; revised 8 October 2009; accepted 12 October 2009)

We present detailed results for the motion of a finite-sized gas bubble in a blood vessel. The bubble (dispersed phase) size is taken to be such as to nearly occlude the vessel. The bulk medium is treated as a shear thinning Casson fluid and contains a soluble surfactant that adsorbs and desorbs from the interface. Three different vessel sizes, corresponding to a small artery, a large arteriole, and a small arteriole, in normal humans, are considered. The haematocrit (volume fraction of RBCs) has been taken to be 0.45. For arteriolar flow, where relevant, the Fahraeus–Lindqvist effect is taken into account. Bubble motion causes temporal and spatial gradients of shear stress at the cell surface lining the vessel wall as the bubble approaches the cell, moves over it and passes it by. Rapid reversals occur in the sign of the shear stress imparted to the cell surface during this motion. Shear stress gradients together with sign reversals are associated with a recirculation vortex at the rear of the moving bubble. The presence of the surfactant reduces the level of the shear stress gradients imparted to the cell surface as compared to an equivalent surfactant-free system. Our numerical results for bubble shapes and wall shear stresses may help explain phenomena observed in experimental studies related to gas embolism, a significant problem in cardiac surgery and decompression sickness.

Key words: blood vessel, embolism, finite-sized bubble motion, front tracking scheme, surfactant

1. Introduction

An understanding of the motion of a gas bubble through a blood vessel is of fundamental importance in gas embolism studies related to illnesses such as decompression sickness. Gas bubbles may enter the blood stream during cardio-pulmonary bypass for cardiac operations or in vascular procedures. This may also happen due to decompression from hyperbaric exposures, such as in diving or extravehicular activity during space exploration. The intravascular gas emboli may deposit into organs, like the heart or the brain, and as a result, cause permanent injury.

A gas bubble moving in a blood vessel may cause damage to the cells lining the interior wall of the vessel (endothelial cells). The mechanisms for the injury appear to be related to the shear stress level imparted and the stress reversals that occur at the cell surface during the bubble motion (Mukundakrishnan, Ayyaswamy & Eckmann 2008*a*). Independently, experiments in our laboratory have shown that such an injury

† Email address for correspondence: ayya@seas.upenn.edu

to the cell may be mitigated by the addition of a soluble surfactant to the continuous phase (Suzuki, Armstead & Eckmann 2004). The surfactant in the blood stream appears to significantly change the dynamics of the bubble–cell interaction (Branger & Eckmann 2002). Furthermore, a non-toxic, soluble, inert surfactant introduced into the bulk phase opportunistically adsorbs onto the gas–liquid interface and modifies the interfacial tension. This results in a change of the bubble shape and its residence time adjacent to the cell surface as compared to an equivalent surfactant-free system. The adsorbed surfactant molecules may also shield biological moieties in the blood stream from encountering the adsorptive surface. The actual mechanisms responsible for this mitigation are not understood, and in this context, an understanding of the role of the surfactant is warranted (Eckmann *et al.* 2006).

In earlier studies, we have experimentally and numerically investigated the motion of a bubble through a surfactant-laden Newtonian fluid and through a blood-like liquid medium (Casson fluid) without the presence of a surfactant (Cavanagh & Eckmann 1999; Eckmann & Lomivorotov 2003; Zhang, Eckmann & Ayyaswamy 2006; Mukundakrishnan *et al.* 2007, 2008*a*; Mukundakrishnan, Eckmann & Ayyaswamy 2008*b*; Mukundakrishnan, Ayyaswamy & Eckmann 2009). Here, through advanced numerical modelling, we investigate the effect of the presence of a soluble surfactant on the motion of a finite-sized gas bubble in a blood vessel.

A number of numerical techniques for treating the motion of a fluid particle or bubble through a surfactant-laden fluid, either soluble (Ghadiali & Gaver 2003; Johnson & Borhan 2003; Muradoglu & Tryggvason 2008) or insoluble (Tsai & Miksis 1994; Li & Pozrikidis 1997; Yon & Pozrikidis 1998; Eggleton, Pawar & Stebe 1999; Eggleton, Tsai & Stebe 2001), have been described in the literature. These are complemented by experimental studies (Rodrigue, De Kee & Chan Man Fong 1996; Branger & Eckmann 1999) and some analyses (Oguz & Sadhal 1988; Park 1992; Milliken & Leal 1994; Rodrigue *et al.* 1999). The numerical methods for the study of free-surface flows include front-tracking or immersed-boundary (Unverdi & Tryggvason 1992; Torres & Brackbill 2000; Shin & Juric 2002), level set (Sussman *et al.* 1999; Osher & Fedkiw 2001), phase-field (Jacqmin 1999), volume-of-fluid (Scardovelli & Zaleski 1999; James & Lowengrub 2004), coupled level-set and volume-of-fluid (Sussman & Puckett 2000), immersed interface (Lee & Leveque 2003), ghost-fluid methods (Udaykumar *et al.* 2003) and moving mesh interface tracking (Quan & Schmidt 2007). Combined experimental and numerical studies examining the rise of a bubble in a surfactant-laden fluid have also been described (Palaparthi, Papageorgiou & Maldarelli 2006).

In this paper, a numerical procedure for evaluating the axisymmetric motion of a nearly occluding gas bubble (the topology of interest to the health sciences) in a surfactant-laden Casson fluid in a cylindrical tube has been described and implemented. The interface of the bubble is tracked using a modified front-tracking method. Flow and species discontinuities are smoothed and the surface tension force is distributed over a thin layer near the interface to become an equivalent volume force. The Navier–Stokes and continuous phase mass-transfer equations are solved on a fixed Eulerian mesh. A level contour reconstruction procedure is employed for the periodic redistribution of the front points and reconstruction of a new front. An explicit background mesh of interconnected marker points is used to represent the interface. Surface convection-diffusion equations are solved on this interface with suitable coupling to the bulk species concentrations to account for interfacial adsorption and desorption.

The properties of the bulk fluid include both the shear-thinning effects of blood and the Fahraeus and Fahraeus–Lindqvist effects (see Ayyaswamy 2008), while the

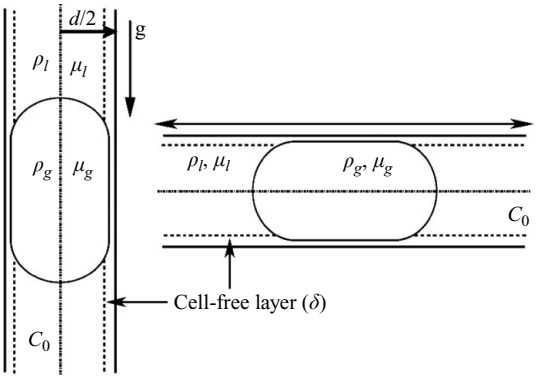

FIGURE 1. Schematic of a nearly occluding bubble in vertical and horizontal vessel configurations.

non-dimensional parameters associated with the surfactant have been broadly chosen from Somasundaran (2006) and Chang & Franses (1995). Results are also provided for a specific case of $C_{12}E_6$ whose properties are provided by Palaparthi *et al.* (2006). The surfactant properties, in general, are similar to those of ethoxylated surfactants and follow the Langmuir isotherm. The specific case of $C_{12}E_6$, however, follows the Frumkin isotherm. Three different vessel sizes, corresponding to a small artery, a large arteriole and a small arteriole in normal humans (Fung 1997), have been considered. The corresponding representative flow Reynolds numbers are 200, 2 and 0.2, respectively. The degree of bubble occlusion is characterized by the ratio of the equivalent-volume bubble radius to vessel radius (aspect ratio), λ, in the range $0.9 \leqslant \lambda \leqslant 1.05$. For non-spherical bubbles, the applicable radius of the bubble is taken to be that of a spherically shaped bubble that has the same volume as the non-spherical one (equivalent-volume spherical radius). The initial bulk flow corresponds to a fully established Casson flow in a cylindrical vessel.

Bubble motion causes temporal and spatial gradients of shear stress at the cell surface lining the blood vessel wall as the bubble approaches the cell, passes over it and departs. Rapid reversals occur in the sign of the shear stress imparted to the cell surface during this motion. Shear stress gradients together with sign reversals are associated with a recirculation vortex at the rear of the bubble. Presence of the surfactant in the bulk and the interface reduces the level of the shear stresses and the strengths of the vortical motions as compared with an equivalent clean system. Furthermore, the shape of the bubble, and consequently the gap between the bubble and the vessel wall, changes in the presence of the surfactant, resulting in a change in the bubble residence time near the proximity of a cell surface. The net effect is to reduce the level or eliminate the mechanically driven injury to the cell surface. The model predictions concur with our experimental findings and are thought to seriously impact gas embolism studies.

The organization of this paper is as follows. The problem formulation is followed by a description of the numerical methodology. The numerical procedure is validated. Detailed computational results are described for the surfactant problem and where necessary comparisons with the clean system study are presented. The final two sections deal with the major results and the important conclusions therein.

2. Problem formulation

The axisymmetric motion of a nearly occluding gas bubble of density ρ_g and viscosity μ_g in a cylindrical vessel of radius R (diameter d) has been considered here

as shown in figure 1. For the vertical configuration of the vessel, gravity acts in the direction from top to bottom.

Both the gas and the liquid phases are modelled as incompressible fluids governed by the equations of motion (Tryggvason *et al.* 2001; Zhang *et al.* 2006):

$$\nabla \cdot \boldsymbol{u} = 0, \tag{2.1}$$

$$\rho\left(\frac{\partial \boldsymbol{u}}{\partial t} + \boldsymbol{u}\cdot\nabla\boldsymbol{u}\right) = -\nabla p + \nabla\cdot\mu(\nabla\boldsymbol{u} + \nabla^T\boldsymbol{u}) + \int_{S(t)}\left[\sigma(\Gamma(s))\mathscr{K}\boldsymbol{n}_f + \frac{\partial\sigma(\Gamma(s))}{\partial s}\boldsymbol{t}_f\right]\hat{\delta}(\boldsymbol{x}-\boldsymbol{x}_f)\mathrm{d}S + \rho\boldsymbol{g}. \tag{2.2}$$

Here, $\boldsymbol{u} \equiv (v_r, v_z)$ is the fluid velocity with v_r, v_z as the velocity components along the radial and axial directions, p is the pressure, ρ and μ are the density and the viscosity of the medium (defined below), $\boldsymbol{g}$ is the gravitational acceleration (9.8 m s^{-2}), s is an arclength measure along the interface, $\mathscr{K}$ is the curvature, σ is the surface tension coefficient and is a function of the surfactant concentration Γ, $S(t)$ denotes the instantaneous location of the interface, $\boldsymbol{n}_f$ and $\boldsymbol{t}_f$ are the unit outward normal and tangential vectors on the interface, $\boldsymbol{x}_f$ denotes the position vector on the interface, and $\hat{\delta}(\boldsymbol{x}-\boldsymbol{x}_f)$ stands for the two-dimensional axisymmetric Dirac delta function that is non-zero only when $\boldsymbol{x}=\boldsymbol{x}_f$. The integral is carried out over the entire surface to create a force on the interface. The density and viscosity of the medium are

$$\rho(r,z,t) = \rho_l\mathscr{H}(r,z,t) + \rho_g(1-\mathscr{H}(r,z,t)), \tag{2.3}$$

$$\mu(r,z,t) = \mu_l\mathscr{H}(r,z,t) + \mu_g(1-\mathscr{H}(r,z,t)). \tag{2.4}$$

Here, t is time, and $\mathscr{H}(r,z,t)$ is a Heaviside function such that

$$\mathscr{H}(r,z,t) = \begin{cases} 1 & (r,z,t) \text{ in the bulk,} \\ 0 & (r,z,t) \text{ in the bubble.} \end{cases} \tag{2.5}$$

The bulk liquid has been modelled as a two-layer fluid of density ρ_l consisting of a cylindrical core of concentrated red blood cell (RBC) suspension, surrounded by a cell-free layer. The cell-free layer is modelled as a Newtonian fluid of constant viscosity μ_{layer} (Sharan & Popel 2001) while the RBC suspension is modelled as a shear-thinning Casson fluid of viscosity μ_c (Fung 1997). The viscosity of the liquid μ_l as a function of the radial position in a bubble-free tube is thus,

$$\mu_l = \begin{cases} \mu_c, & 0 \leqslant r \leqslant (1-\delta)R, \\ \mu_{layer}, & (1-\delta)R < r \leqslant R, \end{cases} \tag{2.6}$$

where δ is the non-dimensional thickness of the cell-free layer normalized with R. The evaluation of this thickness and the two viscosities μ_{layer} and μ_c have been discussed in detail by Mukundakrishnan *et al.* (2008*a*). Following Papanastasiou (1987) and Mukundakrishnan *et al.* (2008*a*), we write

$$\mu_c = \left[\sqrt{\mu_\infty} + \sqrt{\frac{\tau_y}{|\gamma|}}\left(1 - e^{-\sqrt{m|\gamma|}}\right)\right]^2, \tag{2.7}$$

where μ_∞ is the asymptotic Newtonian viscosity, τ_y is the yield stress, γ is the prevalent local shear rate and m is the Casson viscosity regularization exponent. The viscosity of the fluid layer, μ_{layer}, which usually varies as a function of haematocrit is a constant here. More details on the dependence of the viscosity on the haematocrit and the tube size are given in Appendix B.

The surface tension of the interface, separating the continuous and dispersed phases, varies with the surfactant concentration, Γ, on the interface, according to the equation of state given by the Langmuir isotherm (Levich 1962):

$$\sigma = \sigma_s + \Re T \Gamma_\infty \ln\left(1 - \frac{\Gamma}{\Gamma_\infty}\right), \tag{2.8}$$

where σ_s is the surface tension of a surfactant-free clean interface, $\Re$ is the ideal gas constant, T is the absolute temperature and Γ_∞ is the maximum monolayer interface surfactant concentration. The evolution of the surfactant concentration at the interface is given by Stone (1990) as

$$\frac{\partial \Gamma}{\partial t} + \nabla_s \cdot (\boldsymbol{u}_\mathbf{s}\Gamma) + \Gamma\left(\nabla_s \cdot \boldsymbol{n}_f\right)\left(\boldsymbol{u} \cdot \boldsymbol{n}_f\right) = D_s \nabla_s^2 \Gamma + j_n, \tag{2.9}$$

with j_n being the diffusional flux at the interface given by Fick's law: $j_n = D_l(\boldsymbol{n}_f \cdot \nabla)C$. Also, $\boldsymbol{u}_\mathbf{s}$ and $\boldsymbol{u} \cdot \boldsymbol{n}_f$ are the tangential and normal components of the velocity on the interface, respectively, D_s is the surface diffusion coefficient, D_l is the bulk diffusion coefficient, C is the bulk concentration and $\nabla_s = \nabla - \boldsymbol{n}_f(\boldsymbol{n}_f \cdot \nabla)$ is the gradient operator along the interface. The diffusional flux on the interface, $D_l(\boldsymbol{n}_f \cdot \nabla)C$, is balanced by the adsorption and desorption terms as

$$D_l\left(\boldsymbol{n}_f \cdot \nabla\right) C = k_a C_s \left(1 - \frac{\Gamma}{\Gamma_\infty}\right) - k_d \Gamma, \tag{2.10}$$

in which k_a and k_d are the adsorption and desorption coefficients, respectively, and C_s is concentration in the sub-layer adjacent to the interface. The governing equation for the bulk concentration C then becomes

$$\frac{\partial C}{\partial t} + (\boldsymbol{u} \cdot \nabla) C = \nabla \cdot (D \nabla C) - \int_{S(t)} \left[k_a C_s \left(1 - \frac{\Gamma}{\Gamma_\infty}\right) - k_d \Gamma\right] \hat{\delta}(\boldsymbol{x} - \boldsymbol{x}_f) \mathrm{d}S, \tag{2.11}$$

where the diffusion coefficient D may be written as

$$D = D_l \mathscr{H}. \tag{2.12}$$

These equations are coupled with suitable initial and boundary conditions. At the inlet boundary $z = 0$, the velocity profile is a fully developed two-layer Casson profile. This velocity profile and the associated pressure gradient have to be numerically evaluated for each vessel size using the Casson two-layer model ((2.6) and (2.7)) and applicable boundary conditions (see Mukundakrishnan *et al.* 2008*a* for details). These evaluations are based on the maximum flow velocity at the centreline of a bubble-free blood vessel of any given size (Berger, Goldsmith & Lewis 1996). The velocity profile and the associated pressure gradient so calculated are used as inlet boundary conditions. In vivo experimental and clinical literature regarding multi-focal arterial gas embolization as occurs in cardiac surgery and decompression sickness indicates that bubble passage and trapping effects are important within the microcirculatory arteriolar vessels. In this size range, the pulsatility effects of the cardiac cycle on blood flow are much less predominant, so that an approximation of steady flow is reasonable. At the outlet boundary, $z = L$, the outflow condition

$$\frac{\partial \boldsymbol{u}}{\partial z}(r, L, t) = 0 \tag{2.13}$$

is used. The reflective boundary conditions, at $r = 0$, are given as

$$\left.\begin{aligned} v_r(0, z, t) &= 0, \\ \frac{\partial v_z}{\partial r}(0, z, t) &= 0, \\ \frac{\partial C}{\partial r}(0, z, t) &= 0. \end{aligned}\right\} \tag{2.14}$$

The wall no-slip, no flux boundary conditions at $r = R$ are

$$\left.\begin{aligned} \boldsymbol{u}(R, z, t) &= 0, \\ \frac{\partial C}{\partial r}(R, z, t) &= 0. \end{aligned}\right\} \tag{2.15}$$

The initial surfactant concentration in the bulk is taken to be

$$C(r, z, 0) = C_0 \mathscr{H}(r, z, 0). \tag{2.16}$$

3. Non-dimensionalization and time scales

Consider the non-dimensional quantities (denoted by superscripted *): $s^* = s/d$, $r^* = r/d$, $z^* = z/d$, $\rho^* = \rho/\rho_l$, $\boldsymbol{u}^* = \boldsymbol{u}/U_{max}$, $t^* = tU_{max}/d$, $p^* = p/\rho U_{max}^2$, $C^* = C/C_0$, $\Gamma^* = \Gamma/\Gamma_\infty$, $\mathscr{K}^* = d\mathscr{K}$ and $\hat{\delta}^* = d^3\hat{\delta}$. Here, $C_0(\mathrm{mol\,cm^{-3}})$ is the far field bulk concentration and $\Gamma_\infty(\mathrm{mol\,cm^{-2}})$ is the maximum monolayer interface surfactant concentration. Recasting the governing equations (2.2), (2.9) and (2.11) in terms of these non-dimensional parameters (and dropping the superscript * for convenience) yields

$$\frac{\partial \boldsymbol{u}}{\partial t} + \nabla \boldsymbol{u} \cdot \boldsymbol{u} = -\nabla p + \frac{1}{Re}\nabla \cdot \mu(\nabla \boldsymbol{u} + \nabla^T \boldsymbol{u}) + \frac{1}{We} \times \int_S \left[\sigma \mathscr{K} \boldsymbol{n}_f + \frac{\partial \sigma}{\partial s}\boldsymbol{t}_f\right] \hat{\delta}(\boldsymbol{x} - \boldsymbol{x}_f)\mathrm{d}s + \frac{1}{Fr^2}\rho \hat{\boldsymbol{g}}, \tag{3.1}$$

$$\frac{\partial \Gamma}{\partial t} + \nabla_s \cdot (\boldsymbol{u}_s \Gamma) + \Gamma(\nabla_s \cdot \boldsymbol{n}_f)(\boldsymbol{u} \cdot \boldsymbol{n}_f) = \frac{1}{Pe_s}\nabla_s^2 \Gamma + \frac{1}{\alpha Pe}(\boldsymbol{n}_f \cdot \nabla)C, \tag{3.2}$$

$$\frac{\partial C}{\partial t} + (\boldsymbol{u} \cdot \nabla)C = \frac{1}{Pe}\nabla \cdot (D\nabla C) - \int_S [St_a C_s(1 - \Gamma) - \alpha St_d \Gamma]\hat{\delta}(\boldsymbol{x} - \boldsymbol{x}_f)\mathrm{d}s, \tag{3.3}$$

in which the relevant non-dimensional parameters are defined as: Reynolds number $Re = \rho U_{max} d/\mu$, Weber number $We = \rho_l U_{max}^2 d/\sigma$, Froude number $Fr = U_{max}/\sqrt{gd}$, surface Péclet number $Pe_s = U_{max} d/D_s$, desorption Stanton number $St_d = k_d d/U_{max}$, dimensionless adsorption depth $\alpha = \Gamma_\infty/C_0 d$, bulk Péclet number $Pe = U_{max} d/D_l$ and adsorption Stanton number $St_a = k_a/U_{max}$. The capillary number $Ca = \mu U_{max}/\sigma$ is the ratio of Re and We.

Based on these non-dimensional numbers, the important time scales relevant to this problem are convection time scale d/U_{max}, momentum diffusion time scale $\rho d^2/\mu$ and mass diffusion time scales d^2/D_l and d^2/D_s.

4. Numerical method

Equations (2.1)–(2.12), subject to the appropriate initial and boundary conditions ((2.13)–(2.16)), are solved using a front-tracking method coupled with a level contour reconstruction procedure. Briefly, the procedure consists of the

following:

(*a*) Given a particular interface position, and bulk and interface concentration distributions, calculate the surface tension forces and distribute them as body forces to the fixed Eulerian grid.

(*b*) Solve the fluid flow equations with the given conditions to obtain the velocity and pressure fields.

(*c*) Use the computed velocity field to update the interface and bulk surfactant values.

(*d*) Update the position of the interface using the velocity field in a Lagrangian fashion.

(*e*) Reconstruct the interface using the level contour reconstruction procedure if the bubble volume changes by more than 0.5 % or periodically after every few time steps.

(*f*) If the interface is reconstructed, project the surface concentration profile to the new interface in such a way as to conserve the amount of surfactant on the interface.

(*g*) Repeat these steps until either steady state is reached or the bubble reaches the outlet of the computational domain.

A brief description of the procedure follows.

4.1. *Surface tension force redistribution*

The surface tension force, $\boldsymbol{f}_{st}$, acting on a segment of the interface between points A and B can be derived from (2.2) as

$$\boldsymbol{f}_{st} = \int_A^B \left(\sigma \mathscr{K} \boldsymbol{n}_f + \frac{\partial \sigma}{\partial s} \boldsymbol{t}_f \right) \mathrm{d}s. \tag{4.1}$$

Following the use of the Frenet formulae for the unit vectors in the r–z plane as given by James & Lowengrub (2004), this reduces to

$$\boldsymbol{f}_{st} = \int_A^B \left[\frac{\partial}{\partial s} \left(\sigma \boldsymbol{t}_f \right) - \sigma \left(\frac{\partial \boldsymbol{t}_f}{\partial s} + \frac{\boldsymbol{n}_{fr}}{r} \right) \right] \mathrm{d}s, \tag{4.2}$$

where $\boldsymbol{n}_{fr}$ is a vector in the r direction whose length equals the r component of the normal vector, and r is the radial distance. This can then be simplified as (see Mukundakrishnan *et al.* 2007)

$$\boldsymbol{f}_{st} = \sigma_A \boldsymbol{t}_A - \sigma_B \boldsymbol{t}_B - \boldsymbol{e}_r \int_A^B \sigma \, \mathrm{d}s, \tag{4.3}$$

where $\boldsymbol{t}_A$ and $\boldsymbol{t}_B$ are the tangent vectors on the interface at the points A and B, respectively, and $\boldsymbol{e}_r$ is the unit radial vector. To distribute these surface forces onto the fixed Eulerian grid and to avoid any numerical instabilities that may result from high surface tension forces in high density and viscosity ratio flows (Van Sint Annaland *et al.* 2006), a density-weighted function is used. The distributed surface tension force $\boldsymbol{F}_{st}$ is given as

$$\boldsymbol{F}_{st\,(i,j)} = \frac{\sum_e \rho_{i,j} \boldsymbol{f}_{st\,e} D_{i,j}(\boldsymbol{x} - \boldsymbol{x}_m)}{\sum_e \rho_{i,j} D_{i,j}(\boldsymbol{x} - \boldsymbol{x}_m)}, \tag{4.4}$$

where $\boldsymbol{x} = (i\Delta r, j\Delta z)$, $\boldsymbol{x}_m = (r_m, z_m)$ is the mid-point of the interfacial segment e, $\rho_{i,j}$ is the density at the given Eulerian grid point (i, j), and $D_{i,j}$ is

$$D_{i,j}(\boldsymbol{x} - \boldsymbol{x}_m) = \frac{\hat{\delta}\left(r_m/\Delta r - i\right) \hat{\delta}\left(z_m/\Delta z - j\right)}{2\pi r \Delta r \Delta z}. \tag{4.5}$$

The one-dimensional delta function in the above is numerically approximated as (Griffith & Peskin 2005)

$$\hat{\delta}(\hat{d}) = \begin{cases} \hat{\delta}_1(\hat{d}), & |\hat{d}| \leqslant 1, \\ 1/2 - \hat{\delta}_1(2 - |\hat{d}|), & 1 < |\hat{d}| < 2, \\ 0, & |\hat{d}| \geqslant 2, \end{cases} \tag{4.6}$$

and $\hat{\delta}_1(\hat{d}) = (3 - 2|\hat{d}| + \sqrt{1 + 4|\hat{d}| - 4\hat{d}^2 x})/8$. Here, $\hat{d}$ denotes the distance from the origin of the source (the front position).

4.2. *Flow solver*

The unsteady mass and momentum equations are discretized using a second-order finite-difference-based variable density projection method (Sussman & Puckett 2000). The velocity, density and viscosity are all located at cell centres. The time-stepping procedure is based on the second-order Crank–Nicholson method. An intermediate velocity field is obtained using a semi-implicit viscous solver. In this, a second-order predictor–corrector method based on the unsplit Godunov method (Colella 1990) is used to evaluate the advective terms, while a standard second-order central finite difference is used to evaluate the diffusion terms. For the diffusion term, the spatial distribution of viscosity is computed explicitly using the second invariant of strain rate tensor evaluated at the nth time step. Such an evaluation does not impose any additional stability criteria as noted by Radl, Tryggvason & Khinast (2007). The resulting equations for the components of the intermediate velocity are solved by a multi-grid method based on Red–Black Gauss–Siedel smoother (Wesseling 1992). A projection method is invoked on the intermediate velocity to obtain the final divergence-free velocity, the details of which along with the corresponding time step restrictions for numerical stability are given by Sussman & Puckett (2000).

4.3. *Surfactant concentration solver*

The surfactant exchange between the bulk and the interface is modelled as occurring in a thin layer adjacent to the interface (see Muradoglu & Tryggvason 2008). This technique is different from that described in an earlier paper by Zhang *et al.* (2006) wherein this exchange occurs exactly on the interface.

The interface surfactant evolution equation (2.9) is used to update the concentration explicitly. First, the diffusion flux j_n, given in (2.10), is computed in an explicit manner using the previous time step values. The computed diffusion flux is then used in (2.9) to update the interface concentration. This update is done on the Lagrangian grid. The bulk surfactant evolution equation (2.11) is solved on the Eulerian grid. The diffusion flux on the interface is converted to a bulk source term. This is done using a method similar to that used for the distribution of surface tension (see (4.4)). The bulk source term $J_{i,j}$ assumes the form

$$J_{i,j} = \frac{\sum_e \mathscr{H}_{i,j} D_{i,j}(\boldsymbol{x} - \boldsymbol{x}_m) \dfrac{j_{ne} r_e l_e}{r_{i,j} \Delta r \Delta z}}{\sum_e \mathscr{H}_{i,j} D_{i,j}(\boldsymbol{x} - \boldsymbol{x}_m)}, \tag{4.7}$$

where $D_{i,j}(\boldsymbol{x} - \boldsymbol{x}_m)$ is given by (4.5), r_e is the radial distance of the centre of the interface element, l_e is the length of the element, $r_{i,j}$ is the radial distance of the Eulerian grid point and $\mathscr{H}$ is as defined in (2.5). The bulk concentration is then updated explicitly using (2.11).

4.4. *Interface reconstruction*

The redistribution of the front points and the conservation of the bubble volume are simultaneously achieved using a level contour reconstruction procedure (Shin & Juric 2002; Shin *et al.* 2005). As the bubble moves, and especially if the interface significantly deforms, it becomes necessary to recompute the front points defining the interface. Here, this is done in such a way that the final mass (volume) of the bubble, based on the calculation of a new interface, is within 0.5 % of the original volume of the bubble while at the same time minimizing the deviation from the computed advected boundary (see, Mukundakrishnan *et al.* 2007). Upon reconstruction, the new front points are assigned using the intersection of the computed boundary with the Eulerian grid.

4.5. *Interface surfactant projection and mass conservation*

Subsequent to the reconstruction of the interface, the surfactant concentration on the new front points must be recomputed to be consistent with the previous interface points. The surfactant mass on the interface Γ_m must be conserved. The total interface surfactant mass may be written as

$$\Gamma_m|_{total} \approx 2\pi \sum_{i=1}^{n-1} \Gamma_i \left(\frac{r_i + r_{i+1}}{2} \right) (s_{i+1} - s_i), \tag{4.8}$$

where, r is the radial distance in a cylindrical coordinate system measured from the axis of the tube and s_i is the arclength to the ith node point of the interface. For any two points A and B on the old interface, the surfactant mass, spanning across multiple interface segments, is

$$\Gamma_m|_A^B \approx 2\pi \sum_{i=1}^{n-1} \Gamma_i \left(\frac{r_i + r_{i+1}}{2} \right) ((s_{i+1} - s_i) \cap s_{AB}). \tag{4.9}$$

Here, s_{AB} represents the arclength between the two points. Since the total length of the interface itself may change during reconstruction, the equivalent point for A on the new interface, A', is defined by its arclength $s_{A'0}$ as

$$s_{A'0} = s_{A0} \frac{s_{total\_new}}{s_{total\_old}}, \tag{4.10}$$

with a corresponding interface point B' corresponding to B. We conserve the mass locally such that

$$\Gamma_m|_{A'}^{B'} = \Gamma_m|_A^B, \tag{4.11}$$

wherein A, B, A' and B' in general do not coincide with the interface points i. This is achieved by projecting the surfactant mass from each segment of the old interface into the appropriate, scaled new interface segment(s). This mass conservation will automatically satisfy the total mass conservation limit given in (4.8) within computational accuracy, which is verified upon each projection.

5. Validation

Validation for the surfactant-free cases is given by Mukundakrishnan *et al.* (2007, 2008*a*) and will not be repeated here. We have now validated the code in the presence of the surfactant, the details of which are presented in Appendix A.

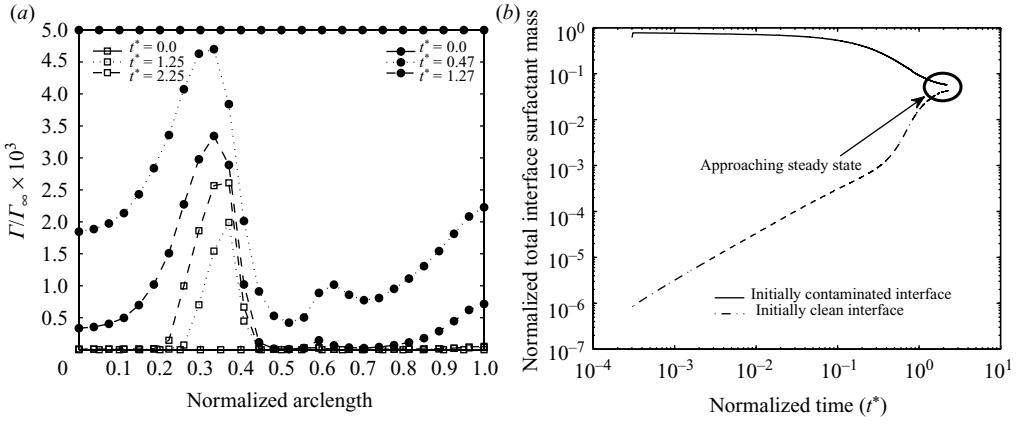

FIGURE 2. Interface concentration profiles at various times for two cases starting from different initial prescribed concentrations. (*a*) Variation of the interface surfactant concentration for various times. (*b*) Variation with time of the total interface surfactant mass. The Reynolds number is 0.2, the dimensionless adsorption depth is 4.75 and the aspect ratio is 1.05. In (*a*), the different symbols indicate the different starting conditions, and the three different line types denote different times. The arclength along the surface of the bubble is measured from the rear stagnation point. In (*b*), the total interface surfactant mass is normalized with $4\pi a^2 \Gamma_\infty$, where a is the equivalent-volume bubble radius.

5.1. *Uniqueness of the steady-state interface concentration*

Here, we examine, for otherwise identical conditions, the time histories of an initially clean bubble and an initially contaminated bubble as they both attain steady states in the surfactant-laden bulk medium. Figures 2(*a*) and 2(*b*) show that in the steady state, the interface concentrations are independent of the imposed initial conditions.

In figure 2(*a*), the interface concentration profile for three different times is shown for both the cases, and with increasing time, both the profiles converge to the same profile. In figure 2(*b*), we observe that the total interface surfactant mass is converging to the same steady-state value starting from the two different initial conditions.

The feature that the eventual steady-state interface concentration is independent from the starting condition is particularly noteworthy. Our numerical experimentation has shown that the computational time to obtain the steady state starting from a clean bubble is considerably larger than that starting with an initially contaminated bubble. Where the transient history is not of concern, for computation it is therefore convenient to start with a slightly contaminated bubble, with an initial shape identical to that of a clean bubble, uniformly coated with the surfactant. This feature becomes particularly advantageous at lower Péclet numbers. In this paper, results for $Re = 0.2$ have been developed using initially contaminated bubbles, thus saving considerable computational time. The characteristics shown in figure 2(*a*) are further discussed in detail in § 6.1.

6. Results

Results for bubble motion in the presence of a soluble surfactant in the bulk phase have been compared with those for an equivalent clean bubble (Mukundakrishnan *et al.* 2008*a*). Fluid flow direction is from the bottom of the vertical vessel towards the top and occurs at a fixed pressure gradient. A soluble surfactant with a far-field concentration of C_0 is assumed to be present in the bulk phase. The bubble rises in

Re	$d(\mu m)$	$U_{max}(\text{cm s}^{-1})$	α	Ca	$Pe = Pe_s$	St_a/St_d
0.2	40	1.75	9.5×10^{-4}	1.225×10^{-3}	1.49×10^{3}	4.5×10^{-5}
2.0	100	7.0	3.8×10^{-4}	4.9×10^{-3}	1.49×10^{4}	1.8×10^{-5}
200	2000	35.0	1.9×10^{-5}	2.45×10^{-2}	1.49×10^{6}	8.9×10^{-7}

TABLE 1. Dimensionless adsorption depths used for the three Reynolds numbers, along with other relevant parameters.

the vessel under the action of body forces (due to gravity) and surface forces (fluid motion) and deforms as it moves.

For all the cases considered here, excepting for the $C_{12}E_6$ surfactant, C_0 is assumed to be the same. This leads to different values of α (see table 1). Table 1 also lists the parameter values for Ca, Pe, and St_a/St_d. The clean interface Ca values are provided in table 1 (Mukundakrishnan *et al.* 2008*a*). All the other properties of the surfactant, including adsorption and desorption coefficients (K_a and K_d), bulk and surface diffusion coefficients (D and D_s) and the maximum interface concentration ($\Gamma_\infty = 1.9 \times 10^{-9}\,\text{mol cm}^{-2}$) are taken to be the same for all the cases considered (except $C_{12}E_6$). The values for the $C_{12}E_6$ surfactant are provided in § 6.5.

Three aspect ratios, λ, have been considered: 0.9, 1.0 and 1.05. For all the cases studied, a thin annular film is assumed to be present between the bubble and the vessel wall at bubble introduction. For $\lambda \geqslant 1.0$, the initial shape of the bubble is assumed to be elongated with a hemispherical cap at each end. The shape, the velocity and the surface concentration of the bubble eventually attain steady states. In this study, we choose to discuss phenomena after the attainment of the steady state.

6.1. *Flow field and concentration profiles*

Figure 3 shows the streamlines for flow over a clean bubble in a reference frame attached to the bubble for various Reynolds numbers and $\lambda = 1.0$. The bubbles are generally deformed with a bulge at the rear primarily due to the imposed pressure gradient. At a certain location along the interface, a very narrow layer of fluid separates the bubble from the wall. This proximity of the bubble to the vessel wall is of particular interest in this problem as shall be seen later. The drainage flow squeezes through this narrow gap and is mainly responsible for the surface mobility of the bubble. This in turn gives rise to internal vortical motions. Secondary internal vortices are also noted and the vortex strengths increase at higher values of Re. The sense of rotation of the secondary vortices is opposite to that of the primary vortex. Two distinct recirculatory bolus formations may be discerned: one at the front region of the bubble and the other at the rear. Two stagnation rings, one convergent ring at the rear and the other divergent ring at the front, exist on the bubble surface where the backflow adjacent to the wall (drainage flow) meets the recirculating boluses. For the convergent stagnation ring (zone), the streamlines move radially outward from near the axis of the tube towards this ring. For the divergent stagnation ring, the streamlines are directed inward towards the axis of the tube. More details for the clean bubble case are available in Mukundakrishnan *et al.* (2008*a*).

Next, we consider bubble motion in a soluble surfactant-laden flow through the vessel. Upon the introduction of the bubble, diffusive and convective mechanisms in the bulk phase will bring the surfactant from the bulk medium to the gas–liquid interface. Here, adsorption and desorption mechanisms will be initiated. Although the vortical motions inside the bubble are essentially similar in their dynamic characteristics to the clean bubble case, they are considerably weaker in strength.

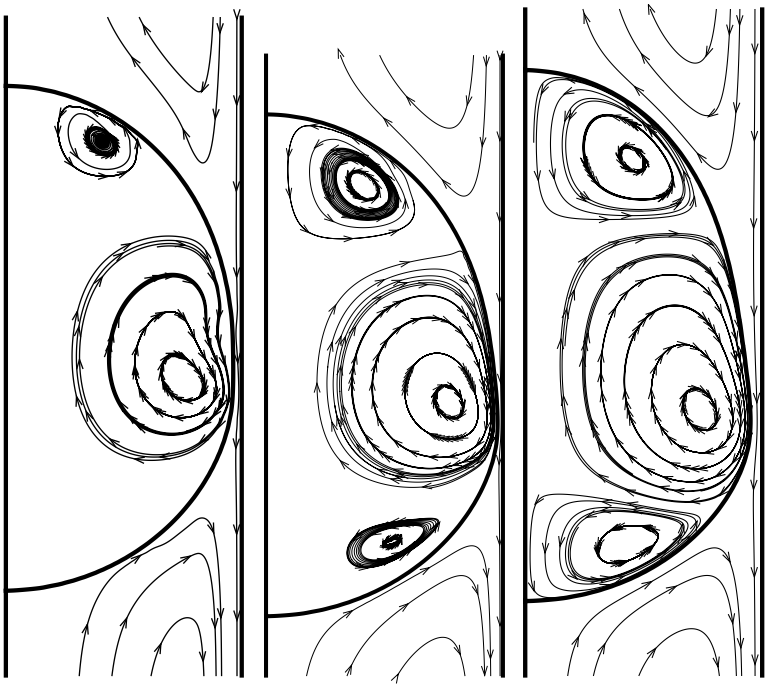

(*a*) $Re = 0.2$. (*b*) $Re = 2.0$. (*c*) $Re = 200$.

FIGURE 3. Streamlines for flow over a clean bubble as viewed in a reference frame moving with the steady-state velocity of the bubble for three representative Reynolds numbers. The aspect ratio (λ) is 1.0.

Diffusion and advection of the adsorbed surfactant occur at the interface, the latter due to surface mobility. Consistent with the bulk concentration and interfacial capacity for adsorption and desorption of the surfactant, a steady-state mass transfer profile is eventually established displaying a non-uniform distribution of the surfactant at the interface.

We now discuss the steady-state concentration profiles at the interface. In an unbounded stationary medium containing a soluble surfactant, the motion of a gas bubble would sweep the surfactant on the interface towards the rear, and the front region will be of higher surface tension (see Sadhal, Ayyaswamy & Chung 1997, Chapter 3). However, for a nearly occluding bubble moving inside a circular tube, the distribution of the surfactant at the interface is complex. In figure 4, we display the steady-state interface concentrations of the surfactant as a function of arclength for various Reynolds numbers. The arclength along the interface is measured starting from the trailing edge of the bubble. In view of the deformed shape of the bubble, the measured arclength is normalized with respect to the total arclength from the trailing edge to the leading edge. At every Reynolds number, the highest and the lowest surfactant concentrations on the interface occur in the vicinity of the convergent and divergent stagnation rings, respectively, accompanied by a complicated distribution elsewhere along the interface.

The attainment of the steady-state concentration profiles may be explained using figure 5, which is a schematic of the streamlines inside and outside the bubble in the reference frame of the bubble. Points A and D in this figure are the rear and front points located on the axis of the bubble, respectively. Points B and C show the approximate locations of the convergent and divergent stagnation rings. Upon the

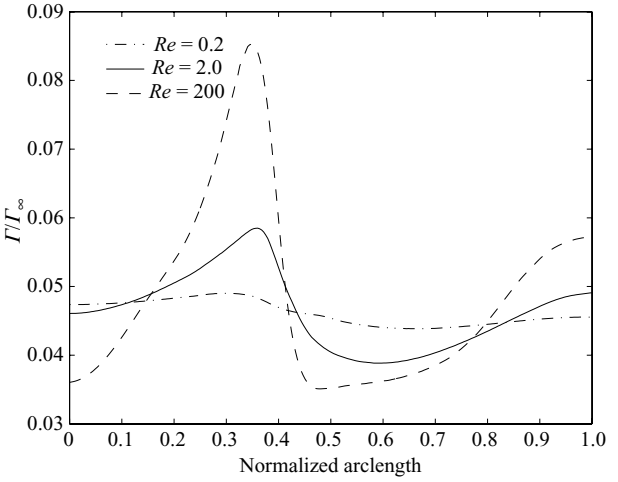

FIGURE 4. Interface concentration for the three cases of Reynolds numbers with identical far-field concentration. The aspect ratio (λ) is 1.0. The normalized arclength along the surface of the bubble is measured from the rear stagnation point.

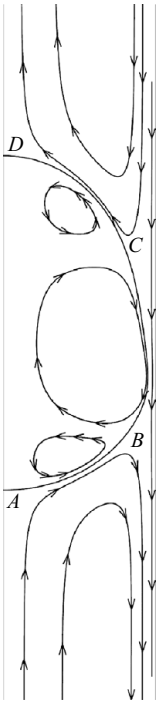

FIGURE 5. Schematic of streamlines.

introduction of the bubble, there will be increased accumulation of the surfactant in the vicinity of A relative to that near D. The prevailing interface convection will sweep the surfactant from A towards B. On the bubble front, surfactant will be swept by the incoming flow towards C. From C, interface convection moves the surfactant towards D and B. The drainage flow will sweep the surfactant deposited between B and C towards B. Thus, at B, there is increased accumulation due to contributions from both A and C. The accumulation of surfactant at B and depletion at C will set

up interface concentration gradients. This leads to surface diffusion (measured by the surface Péclet number Pe_s) which will tend to equalize the surfactant distribution. The final concentration profile is thus determined by the interplay between these various mechanisms. The surfactant boundary layer in this problem is very small compared with the bubble diameter for all three Reynolds numbers considered. This is consistent with the high values of bulk Péclet number, Pe (see table 1). There is negligible variation in the value of the bulk surfactant concentration level near the vessel wall. Our computations show this variation to be less than 1 %.

A major effect of the presence of the surfactant on the bubble surface is the reduction in surface mobility. As the bubble moves, an internal vortex is formed (somewhat similar to a Hill's spherical vortex (Happel & Brenner 1983), or more generally a toroidal vortex). A surfactant coating changes the properties (shape and strength) of this vortex (Johnson & Sadhal 1983; Sadhal & Johnson 1983). The streamlines for a clean and a surfactant-coated bubble as viewed in an inertial frame of reference, for $\lambda = 1.0$, are shown in figure 6 for various Reynolds numbers. Presence of the surfactant causes the recirculation vortex noted here to be weaker as evident from the increased distortion of the streamlines for the clean bubble case.

A measure of the internal circulation in the bubble is given by the strength of the vortex tube(s) (see Batchelor 1967, § 2.6) and is $\int \omega \mathrm{d}V$, where ω is the vorticity, $\mathrm{d}V$ is an elemental volume. The integral is carried out over the volume of the bubble. The ratio of the strengths of the vortex tubes between a clean and a surfactant-coated bubble is shown in figure 7 for various Reynolds numbers. The strength of the toroidal vortices present in the bubble (figure 3) decreases upon the addition of a surfactant. The reduction in vortex strength is the lowest for the largest Reynolds number considered here (200) where the inertial forces are dominant.

6.2. *Steady-state shape*

A detailed study of the steady-state shapes of clean bubbles in motion has been described by Mukundakrishnan *et al.* (2008*a*). Briefly, at smaller Reynolds numbers (0.2 and 2), the capillary effects dominate over the inertial and viscous effects. For these two Reynolds numbers, for $\lambda = 0.9$, the bubble essentially remains spherical, while for $\lambda \geqslant 1.0$, it nearly occludes the vessel. At the higher Reynolds number (200), inertial forces dominate. At $\lambda = 0.9$ bubbles form a flatter interface at the rear and are prolate spheroidal at the front. For $\lambda \geqslant 1.0$, the bubble elongates in the axial direction due to the increased wall effects accompanying the inertial forces.

Figure 8 shows the variations in the shapes of surfactant-coated bubbles as compared with clean bubbles. There are three primary surface forces that affect the shape of the nearly occluding bubble. The first is the surface tension on the interface of the bubble and this tends to make the bubble spherical. The second is a result of the prevailing pressure gradient driving the flow. This force will tend to 'flatten' the bubble in the rear causing it to be oblate spheroidal. The third force arises due to the presence of the wall. As the bubble gets closer to the wall, the drainage flow generates a force that acts to push the sides of the bubble radially inward, away from the wall causing it to elongate in the direction of its motion. The final shape of the bubble is the result of a balance of these three forces together with the body force (buoyancy). However, the body force does not play a major role in this problem as shown later. Reduction in the value of the surface tension due to the surfactant results in increased departure from sphericity and the bubble shape is more responsive to fluid flow-induced deformation forces.

For $\lambda = 0.9$ (see figure 8*a*,*d*,*g*), a clean bubble is nearly spherical with a larger gap between the interface and the vessel wall. The forces that mainly govern the shape of

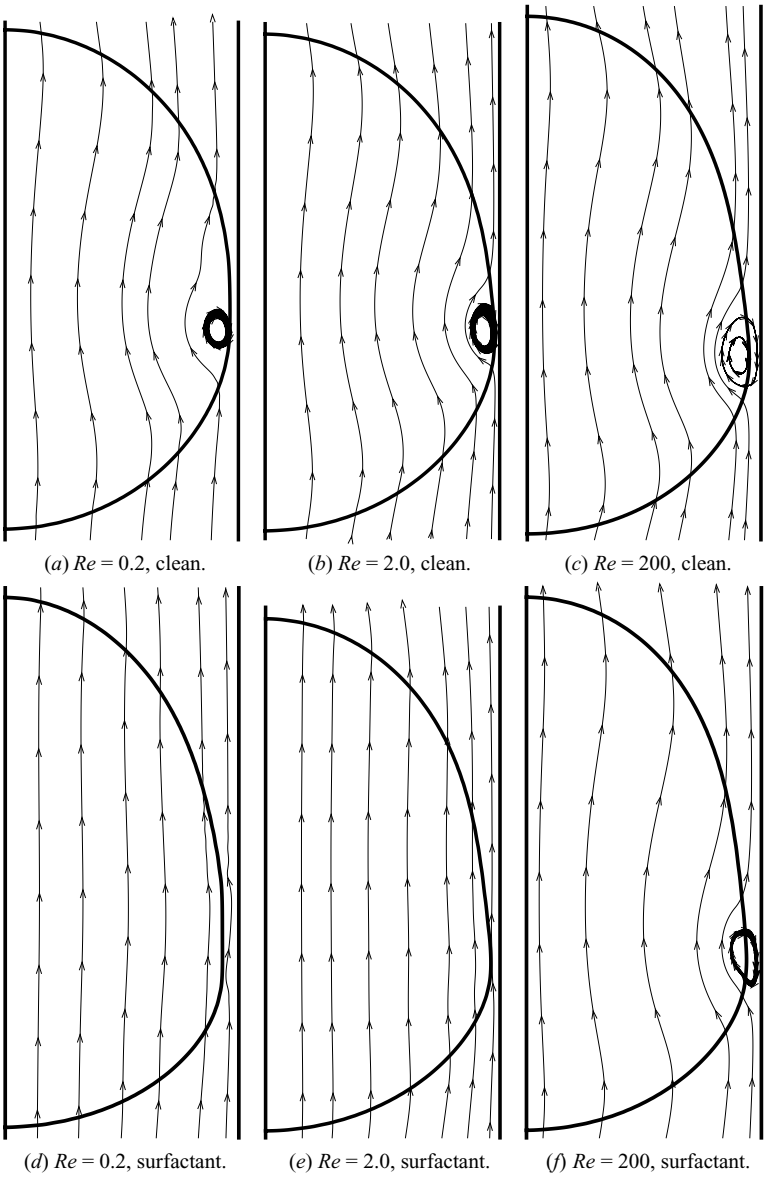

FIGURE 6. Streamlines as viewed in an inertial reference frame for clean and surfactant-coated bubbles. The aspect ratio (λ) is 1.0.

the bubble are the imposed pressure force, tending to flatten the bubble at the rear and the surface tension force that acts to preserve its sphericity. Reduction in surface tension results in an oblong shape. However, for $\lambda \geqslant 1.0$, for a clean bubble, all the three surface forces are significant since the bubble interface is closer to the wall. The radially inward force arising from the drainage flow becomes more important in this case because the fluid is being squeezed through a narrower gap, and this force acts to elongate the bubble in the direction of its motion, resulting in an elongated oblong shaped bubble. In the presence of a surfactant, the imposed pressure force flattens the rear of the bubble farther, while the force due to the draining flow acts to counter this. The result is that the minimum gap between the interface and the wall actually increases.

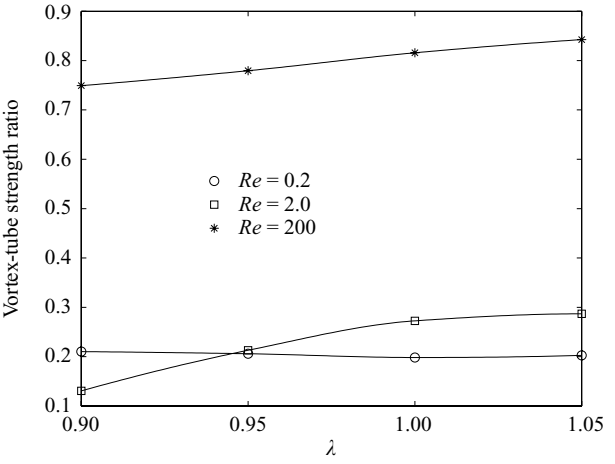

FIGURE 7. Variation of the ratio of the vortex-tube strengths between a clean and surfactant-coated bubble, as a function of the aspect ratio for three Reynolds number cases.

The non-sphericity index, (η), of the bubble may be defined by the ratio of twice the maximum radial extent of the bubble, as measured perpendicular from the axis of the vessel, to its axial length. For a spherical bubble, η is 1.0, although $\eta = 1.0$ does not always imply sphericity. For axially elongated bubbles, η is less than 1, while for radially flattened bubbles, η is greater than 1. Figure 9 shows the variation of η with λ, at various Reynolds numbers, for a clean and surfactant-coated bubble.

From figures 8 and 9, for Reynolds number 200, the inertial forces are noted to be dominant for both the clean and the surfactant-coated bubbles. The value of η decreases in the presence of the surfactant but the shape of the bubble does not change much. For Reynolds numbers 0.2 and 2 and $\lambda \geqslant 1.0$, with a lowered surface tension, the wall effects become more pronounced and the interface is pushed radially inward causing a lowering of η. This indicates that the bubble has axially elongated. For $\lambda = 0.9$, η does not change appreciably. As the rear of the bubble flattens due to the imposed pressure, the gap between the bubble and the vessel wall decreases resulting in increased wall effects that counter this flattening.

The change in the bubble shape may also be evaluated in terms of the minimum gap size between the bubble and the tube wall, and the length of the bubble, as shown in figures 10(a) and 10(b), respectively. This gap will impact the flow field near the wall and the magnitude of the shear stress experienced by the cells lining the interior of the vessel wall. Thus, the minimum gap size is an important parameter to be considered in the gas embolism problem. Both shear and normal stresses applied to endothelial cells are known to produce membrane stretch and induce intracellular calcium (Ca2+) signalling (Sigurdson, Sachs & Diamond 1993; Oike, Droogmans & Nilius 1994). This is also observed by one of the authors (DME) in *in-vitro* studies of cell/bubble interactions.

6.3. *Velocity and stress variation*

Bubble length (figure 10b) and its velocity determine the duration of time during which any given point located on the vessel wall will experience the effect of the bubble passing over it (bubble residence time). The variation in the steady velocity of the bubble in the presence of the surfactant is shown in figure 11. This velocity has been normalized with reference to that for a corresponding clean bubble.

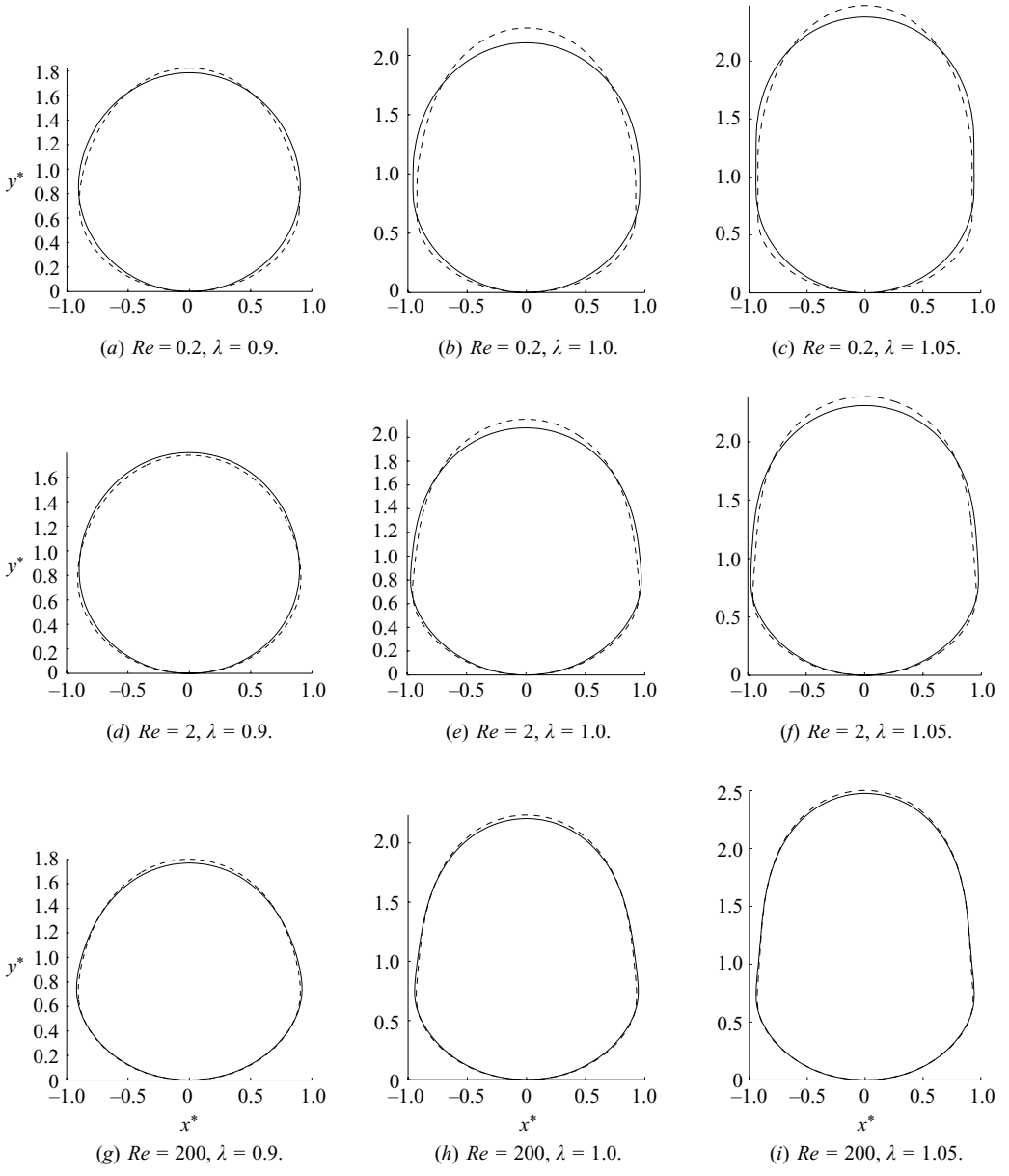

FIGURE 8. Comparison of the steady-state shape of an occluded bubble with and without interfacial surfactants. The solid line represents the shape of the clean interface bubble, while the dotted line represents a surfactant-coated bubble.

In general, a bubble moving in an infinite medium will experience increased retardation in the presence of a surfactant (Bond & Newton 1928) primarily through the set-up of tangential surface tension gradients (Marangoni forces). It will therefore move at a lower velocity compared with that of a clean bubble. In our problem of a deformed nearly occluding bubble in a confined flow, the steady-state velocity will significantly depend on its shape. For a given inlet velocity, up to $\lambda = 1.0$, the occlusion and the profile drag increase causing a reduction in the steady velocity. Beyond $\lambda \geqslant 1.0$, the behaviour is complicated. From figure 11, for $Re = 200$, the normalized bubble

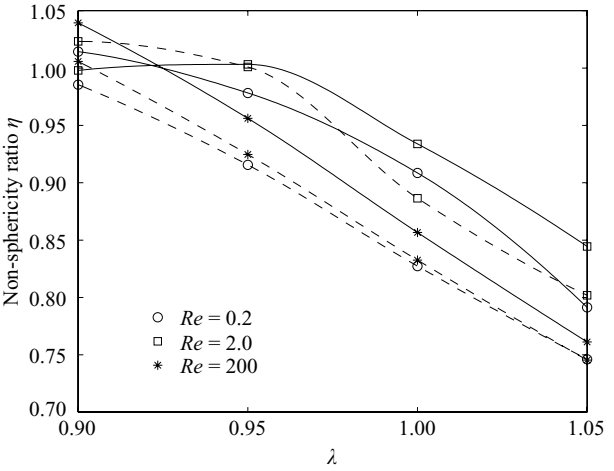

FIGURE 9. Variation in the non-sphericity (η) of the bubble upon the introduction of a surfactant as a function of the aspect ratio for the three different Reynolds numbers. The solid line indicates a clean bubble, while the dashed line indicates a surfactant-coated bubble.

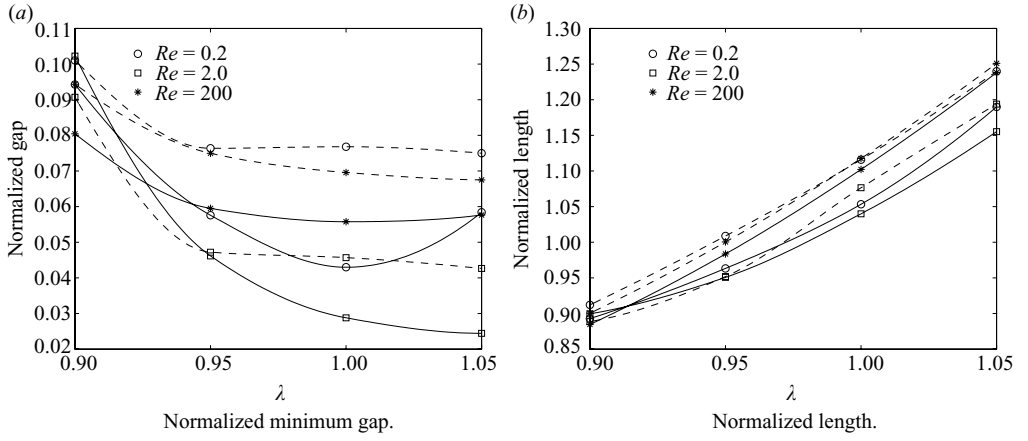

FIGURE 10. Variation in the normalized minimum gap and normalized length of the bubble upon the introduction of a surfactant as a function of the aspect ratio for the three different Reynolds number ratios. The solid line indicates a clean bubble, while the dashed line indicates a surfactant-coated bubble. The gap is normalized with the vessel radius and the length is normalized with vessel diameter.

velocity increases, although not significantly. In the presence of the surfactant, there is very little change in the shape of the bubble (form drag is reduced slightly compared with an equivalent clean bubble) at this Reynolds number (figure 9). The inertial forces dominate the Marangoni forces, resulting in increased speed. For $Re = 2$ and $\lambda < 1.0$, the inertial forces are of the same order as viscous forces, and the Maragoni force slows down the bubble. But with increasing λ, the surfactant effect is such as to cause an elongation of the bubble in the axial direction. This increases the speed of the bubble and for $\lambda > 1.0$, it moves faster than a corresponding clean bubble, although this increase in speed is small. For $Re = 0.2$ and $\lambda < 0.97$, viscous forces dominate. Together with Maragoni forces, there is a reduction in the bubble speed. However, beyond $\lambda \sim 0.97$, bubble elongation causes it to speed up relative to a clean bubble. But, for $\lambda > 1.0$ there are competing effects between the shape change at the

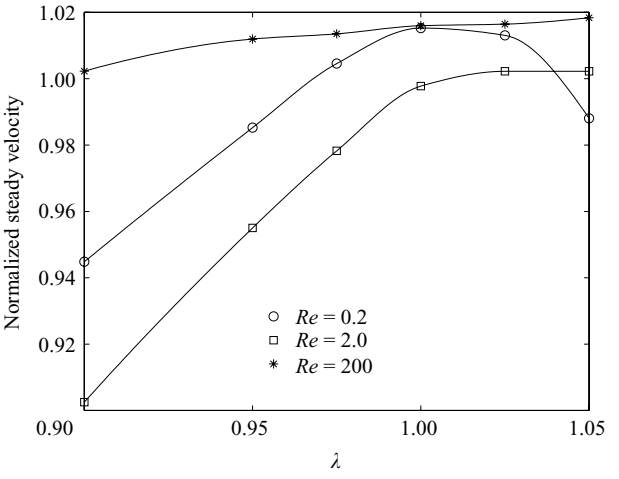

FIGURE 11. Normalized steady velocity of the bubble for three different Reynolds numbers as a function of aspect ratio. The normalization has been done with the velocity for a corresponding clean bubble. The clean bubble velocities (in $\mathrm{cm\,s^{-1}}$) for the three Reynolds numbers 0.2, 2 and 200 are 1.31, 4.5 and 20.65, respectively.

rear (bulging) and the elongation in the axial direction. Around $\lambda > 1.02$, the shape change at the rear is responsible for the slowing down of the bubble compared with a clean one.

An important quantity of interest is the time variation of the shear stress τ at any given point on the vessel wall as the bubble approaches, moves over this point and departs. As the bubble moves, the entrained fluid surrounding it causes rapid changes in the magnitude and the sign of the shear stresses experienced by the wall. For a given point on the wall, the changes in shear stress manifest as a solitary wave (see Mukundakrishnan *et al.* 2008*a* for discussions related to a clean bubble). Briefly, the shear stress variation occurs as follows. When the bubble is far upstream from the point under consideration, it has negligible effect on this point and the shear stress is at its basal value. As the bubble moves closer to the point, the local fluid velocity is increased. Both the local pressure gradient and the flow rate at the location of this point attain higher values and there is a corresponding increase in the shear stress. As the bubble moves over the point, the flow decelerates due to entrainment and the shear stress gradually reduces to zero. The local pressure gradient reverses from being favourable to adverse during this period. As the maximum bulge in the bubble passes over the point, a local flow reversal occurs due to the presence of the recirculating vortex (see figure 6). This vortex arises due to the drainage flow interacting with the forward flow. These interactive effects are ascribable due to the finite size of the bubble and the resultant physical interplay of the trailing gas–liquid interface and the presence of the wall. In particular, the sign of the shear stress becomes negative. Beyond this, as the maximum bulge of the bubble departs the location, there is fluid flow recovery and a significant increase in local fluid velocity in the direction of motion of the bubble. This causes the shear stress to become positive and attain a value higher than its basal value. As the bubble moves farther away from the point, the entrainment effects become progressively weaker and the shear stress gradually returns to the basal value staying there for the remainder of the motion of the bubble. This solitary wave has major potential physiological implications including induction of a complex pattern of endothelial cell membrane stretch and compression, activation

of mechanotransduction pathways, loss of plasma membrane integrity and plasma membrane stress failure (McNeil & Steinhardt 1997; Vlahakis & Hubmayr 2000; Butler *et al.* 2001; Huang, Kamm & Lee 2004; Mendez, Rickman & Hubmayr 2004).

A comparison of the shear stresses experienced by a point on the vessel wall, for clean and surfactant-coated bubble motions, is shown in figure 12. The shear stress is normalized with the corresponding base value, τ_{ref}. As seen in figure 6, the recirculating vortex is significantly weakened by the presence of the surfactant. As a result, the variations in shear stresses, although following a behaviour similar to that for a clean bubble, are considerably lower in magnitude. In figure 12, only the duration of time where there is significant deviation in the stress from its basal value is displayed, and this period corresponds to the motion of the bubble over the point. The effect of the surfactant is more pronounced at the lower two values of Reynolds numbers (0.2 and 2), while for $Re = 200$, the profile of the solitary wave does not change much from that for a corresponding clean bubble. This can be explained by noting that a decrease in Reynolds number corresponds to a decrease in the surface mobility of the bubble. In turn, the recirculating vortex that is primarily responsible for causing the stress reversals is also weaker. Furthermore, as previously discussed, for $\lambda \geqslant 1.0$, the presence of the surfactant increases the minimum gap size between the bubble interface and the vessel wall. This increase in the minimum gap size is more pronounced at lower Reynolds numbers (see figure 10*a*), resulting in reduced shear stress variations. The presence of the surfactant will therefore have predominant effects at lower Reynolds numbers.

In figure 13, the jump in the value of the shear stress, $\Delta\tau = \tau_{max} - \tau_{min}$, has been plotted as a function of λ for various Reynolds numbers. The corresponding clean bubble results are also given for comparison. The value of $\Delta\tau$ is an index of the magnitude of the shear stress change to which the luminal endothelial cell surface is subjected. The time rate of change of $\Delta\tau$ is a measure of the impulse character of the solitary wave as it traverses the cell surface. Together they provide a mechanism for cell injury by rapid bidirectional stretching of the cell surface. In vivo observations of surfactants attenuating gas embolism-associated impairment of vessel tone regulatory function mediated by endothelial cells have been recorded (Branger & Eckmann 2002). It may be seen from the figure that the decrease in the value of $\Delta\tau$ is more pronounced for $Re = 0.2$ and $\lambda > 1.0$. This confirms observations from figure 12. The reduction in the value of $\Delta\tau$ is due to both the weakening of the recirculation vortex (figure 6) and the change in shape of the bubble (figure 8). At lower Reynolds numbers, in the presence of a surfactant, bubbles with $\lambda \geqslant 1.0$ tend to be farther away from the proximity to vessel wall compared with a corresponding clean bubble (figure 10*a*). As a result, there is a reduction of the bubble effect on the wall. The protective surfactant effects to reduce cellular injury or death have occurred in vessels of a size corresponding to lower Reynolds numbers as predicted here.

6.4. *Comparison with horizontal configuration*

Thus far, we have reported on the motion of a bubble in a vertical tube. In this section, a comparison is provided with the results for a bubble moving under identical conditions in a horizontal tube. The representative Reynolds number is taken to be 2 and the aspect ratio $\lambda = 1.0$. The comparisons for the shear stress level and the interface concentration are shown in figure 14.

The results for the steady velocity of the bubble, the flow patterns and shear stress levels from the horizontal configuration are nearly identical to those for the vertical geometry. This confirms that at the levels of pressure drops considered for the forced flow, buoyancy effects are negligible in this problem.

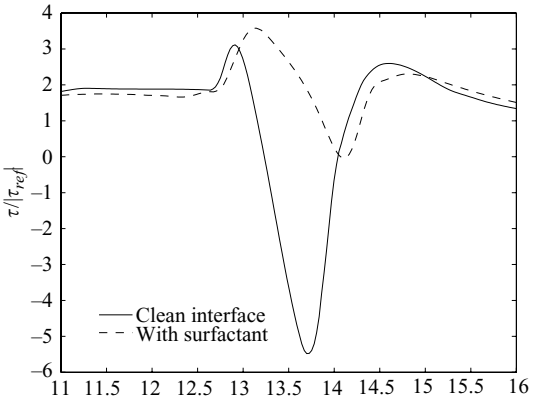

(*a*) $Re = 0.2$, $\tau_{ref} = 56$ dyn cm^{-2}.

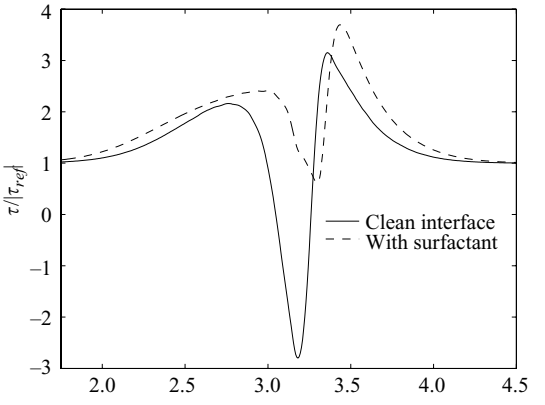

(*b*) $Re = 2$, $\tau_{ref} = 104$ dyn cm^{-2}.

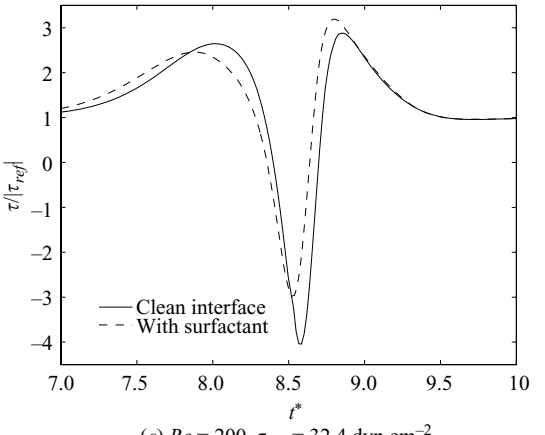

(*c*) $Re = 200$, $\tau_{ref} = 32.4$ dyn cm^{-2}.

FIGURE 12. Variation of shear stress at a point on the vessel wall as the bubble passes over it. The normalization of the shear stress is done with the corresponding basal value. λ is 1.0.

6.5. *Comparison with $C_{12}E_6$ surfactant*

The properties of the surfactant stated in table 1 have been chosen from a broad range of ethoxyl group surfactants given by Chang & Franses (1995). In order to demonstrate the validity of our results with a different surfactant, we now simulate

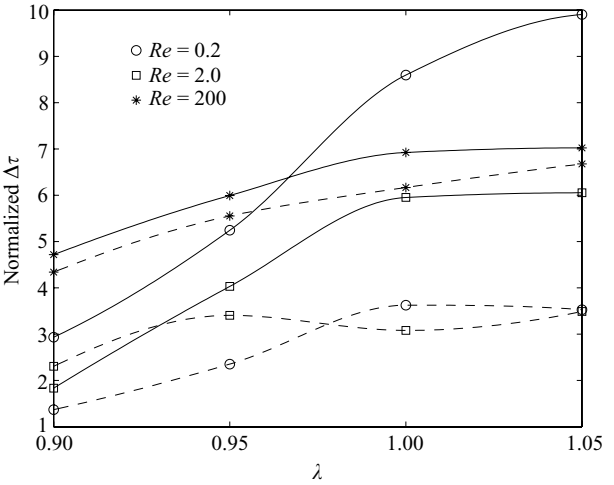

FIGURE 13. Variation of the difference between the maximum and minimum shear stresses experienced by a point on the vessel wall. The normalization of the shear stress is done with the corresponding base value. The solid line represents the clean interface and the dashed line represents the surfactant-coated interface.

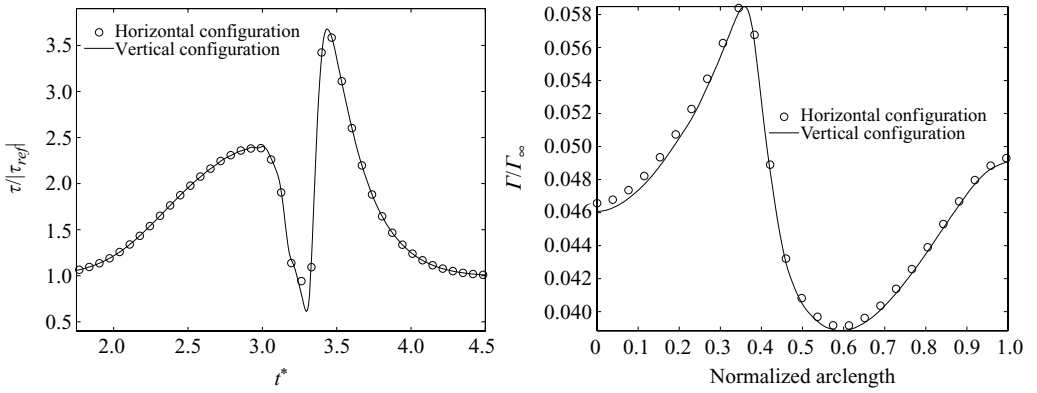

(*a*) Shear stress. (*b*) Interface concentration.

FIGURE 14. Comparison of the shear stress level and interfacial surfactant concentration profiles between a horizontal and a vertical tube. The flow Reynolds number is 2.0 and the aspect ratio is 1.0. The Froude number is ∼0.71.

the motion of a bubble in the presence of hexaethylene glycol dodecyl ether ($C_{12}E_6$). From Palaparthi *et al.* (2006), we have obtained the relevant parameter values for the surfactant $C_{12}E_6$ and carried out the simulation for $Re = 2$. All surfactant properties, except for the diffusivity (which will be higher in blood than in glycerol–water mixture), are assumed to be identical to those obtained for the 70:30 glycerol–water mixture listed therein. In this simulation, C_0 is 0.2 mol m^{-3} (this is assumed to be less than the critical micelle concentration, reported as 0.209 mol m^{-3} by Palaparthi *et al.* 2006), Γ_∞ is 5×10^{-6} mol m^{-2}, both D_l and D_s are 1.3×10^{-10} m^2 sec^{-1} (this value is from Chang & Franses 1995), K_d is 9×10^{-3} sec^{-1} and K_a is 5×10^{-5} m sec^{-1}. The equation of state for this surfactant is the Frumkin isotherm (in contrast to the

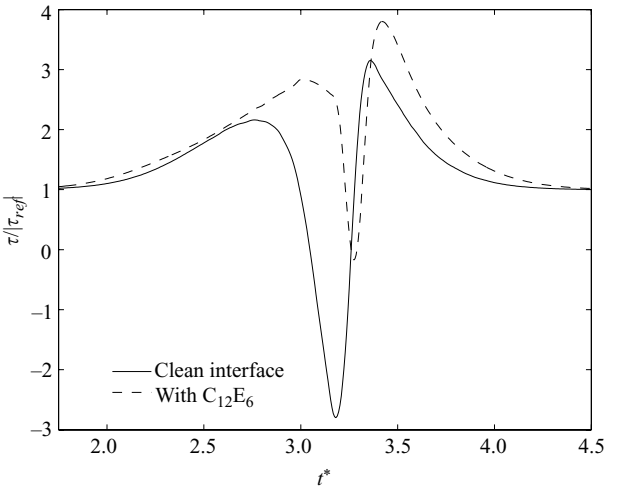

FIGURE 15. Variation of shear stress at a point on the vessel wall as the bubble passes over it, with and without the presence of the surfactant $C_{12}E_6$. The normalization of the shear stress is done with the corresponding basal value. $\lambda = 1.0$ and $Re = 2$.

Langmuir isotherm used thus far) and is given by

$$\sigma = \sigma_s + \Re T \Gamma_\infty \left(\ln\left(1 - \frac{\Gamma}{\Gamma_\infty}\right) + \frac{\xi}{2}\left(\frac{\Gamma}{\Gamma_\infty}\right)^2 \right), \tag{6.1}$$

where ξ is the Frumkin interaction parameter and is set at 5.47 in our simulation (Palaparthi *et al.* 2006). A comparison of the shear stress experienced by a point on the vessel wall, with and without the presence of the surfactant $C_{12}E_6$, is shown in figure 15.

The characteristics displayed in figure 15 show that the predictions follow the same trends that are observed with other surfactants, although there is a quantitative difference (compared with figure 12*b*). This gives us confidence in the validity of our results.

6.6. *Surfactant concentration effect*

Thus far, we have examined bubble motion at a given far-field bulk surfactant concentration level. This has helped us to delineate the role of the surfactant on the bubble motion and to compare the results with an equivalent clean bubble case. The comparisons have shown that the presence of the surfactant helps in lowering the shear stress level imparted to the endothelial cell surface and prevent or minimize injury. However, it is important to examine the behaviour of differing bulk concentration levels of the surfactant in order to identify the most suitable concentration for application purposes. Towards this objective, we are embarked upon a systematic study of various concentration levels in the bulk phase. Herein we provide an illustrative result in figure 16 that shows the variation of the difference between the maximum and minimum shear stresses experienced by a point on the vessel wall for the three different Reynolds numbers, as a function of the dimensionless adsorption depths α.

At a given *Re*, an increase in α denotes a decrease in C_0, the bulk concentration of the surfactant. Here $\Delta\tau$ is noted to decrease with increasing C_0, and this indicates that the shear stress levels are increasingly attenuated at larger C_0 values. The recirculation vortex strengths decrease with C_0. Therefore, higher levels of C_0 would be preferable

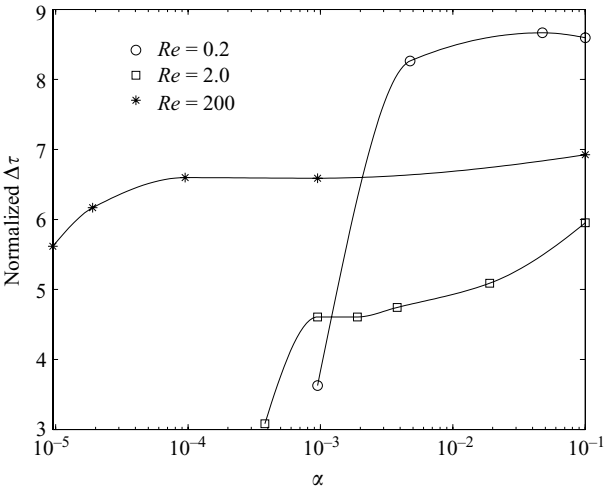

FIGURE 16. Variation of the difference between the maximum and minimum shear stresses experienced by a point on the vessel wall for different values of the dimensionless adsorption depths. The normalization of the shear stress is done with the corresponding base value. The aspect ratio is fixed at 1.0.

from cell injury viewpoint, although other effects such as toxicity may have to be considered. In Swaminathan, Ayyaswamy & Eckmann (2009), a more detailed study will be presented.

7. Conclusions

A numerical method for the evaluation of the axisymmetric motion of a finite-sized, nearly occluding gas bubble in a blood vessel containing a soluble surfactant in the bulk medium has been described and implemented. Convective and diffusive mechanisms, both in the bulk medium and on the interface, have been considered. The surfactant adsorbs onto and desorbs from the interface as governed by interfacial thermodynamics. The effect of the presence of the surfactant in the bulk medium on the motion of the bubble has been systematically examined by comparing the characteristics of the results with those for an equivalent surfactant-free clean bubble motion. This comparison allows for a better understanding of exogenous surfactant-based intervention of gas embolism. The main observations include:

(*a*) Multiple intravital microscopy studies (Branger & Eckmann 1999, 2002; Eckmann & Lomivorotov 2003; Eckmann, Kobayashi & Li 2005) have shown that microvascular gas embolism bubbles deposit with an elongated sausage-shaped geometry (i.e. $\lambda > 1$) into blood vessels. We have shown here that all the three surface forces are significant for this configuration, especially for clean bubbles close to the wall. A major resultant effect is the propagation of a shear stress solitary wave along the wall caused by the bubble, bulk fluid and interfacial motion. This spatially and temporally varying shear stress wave is likely responsible for having induced the injurious or lethal membrane stretch of endothelial cells lining the vasculature observed during in vivo experiments of gas embolism (Eckmann & Armstead 2006) and is consistent with other membrane stretch mechanisms of cell death (McKinney *et al.* 1996; Liu *et al.* 2002). We have herein demonstrated that the presence of a surfactant dramatically and beneficially alters the shear stress, yielding an important cellular mechanoprotective influence that may have a substantial clinical role in the

prevention of gas embolism-related tissue injury, a significant problem in cardiac surgery and decompression sickness.

(*b*) The surfactant is shown to opportunistically adsorb onto the gas–liquid interface. This modifies the interfacial tension resulting in a change of the bubble shape and its residence time adjacent to the cell surface. Residence time of the bubble adjacent to an endothelial cell is a critical quantity in gas embolism. Experimental studies have shown that this time determines cell response.

(*c*) The pressure-driven flow causes the bubble to deform with a bulge at the rear. A drainage flow squeezes through the narrow gap between the bubble and the wall. This flow is primarily responsible for the surface mobility of the bubble and vortical motions. We have shown that the strengths of the recirculation and the vortical motions are reduced by the presence of the surfactant.

(*d*) For a given bulk concentration level of the surfactant chosen here, the effect of the surfactant is shown to be most prominent in the small arteriole, followed by the large arteriole, and is least for the small artery.

This work was sponsored by the Office of Naval Research Grant N00014-08-1-0436, NIH Grant R01-HL067986 and NASA Grant N00014-08-1-0436. The authors also thank one of the reviewers for helpful insights.

Appendix A. Validation

A.1. *Interface diffusion*

The first validation involves the role of the diffusive terms in the surfactant concentration equation at the interface (see (2.9)). The algorithm is tested for a stationary spherical bubble with only the interface diffusion term enabled. Initially, a prescribed variation in the distribution of the interface concentration given by

$$\Gamma(\theta, t) = \frac{1}{2}(1 - \cos\theta) \tag{A 1}$$

is assumed. This surfactant is insoluble. The bubble is assumed to be in an infinite medium (bounding walls are set to be very far away from the bubble). The interface has no additional source term. The interface concentration is then evaluated as a function of time. The number of grid points along the interface and time step restrictions are chosen as in Zhang *et al.* (2006). An analytical solution to this problem is given by James & Lowengrub (2004) as

$$\Gamma(\theta, t) = \frac{1}{2}\left(1 - \cos\theta \exp\left[\frac{-2t^*}{Pe_s}\right]\right), \tag{A 2}$$

where, for this comparison, we define $Pe_s = Ua/D_s$ as the surface Péclet number, $t^* = tU/a$ is the non-dimensional time scale, U is a velocity scale and a is the radius of the bubble. A comparison of the analytical solution with the present numerical results is displayed in figure 17. Our numerical prediction agrees well with the analytical solution in this case.

A.2. *Bulk diffusion and mass transfer*

The next validation considers an initially clean bubble of radius a, placed in a stationary medium with a uniform soluble surfactant concentration C_0. The interface concentration Γ as a function of time t for a given diffusion coefficient D_s is calculated. The analytical solution to this problem is given by Muradoglu & Tryggvason (2008)

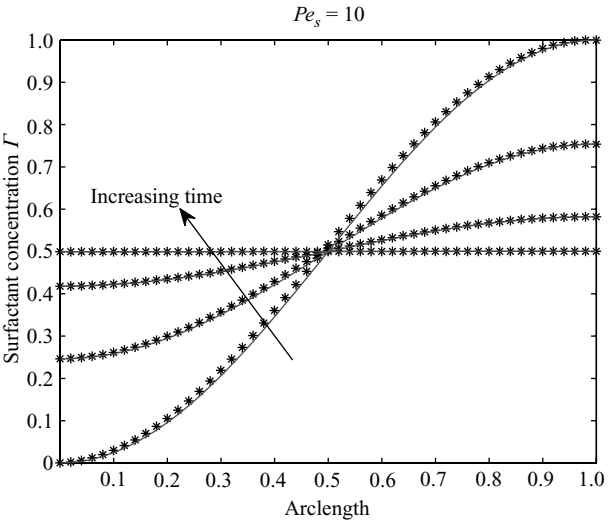

FIGURE 17. Concentration on the interface of a spherical bubble, with an initial surfactant distribution, placed in an infinite medium for various times. The four lines correspond to $t^* = 0$, 3.9, 9.0 and 34. The solid line corresponds to the analytical solution and the '*' symbols correspond to our numerical results.

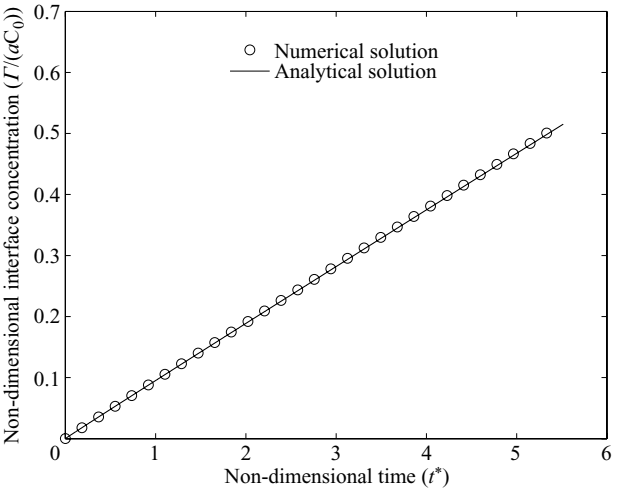

FIGURE 18. Interface concentration as a function of time for an initially clean bubble placed in a bulk medium with uniform initial surfactant concentration. The analytical result is from Muradoglu & Tryggvason (2008).

as

$$\Gamma = k_a C_0 \left(t - \frac{\omega h}{\eta^3} \left(\eta^2 t - 2\eta\sqrt{t} + 2\ln\left(1 + \eta\sqrt{t}\right)\right)\right), \tag{A 3}$$

where k_a is the adsorption coefficient, $\omega = k_a/D_s$, $h = \sqrt{\pi D_s}$ and $\eta = \frac{h}{a}(1 + \omega a)$. The desorption coefficient is set equal to zero. The comparison between the analytical result and the present numerical computation is shown in figure 18. Figure 19(a) shows a comparison between the analytical and numerical values of the concentration of

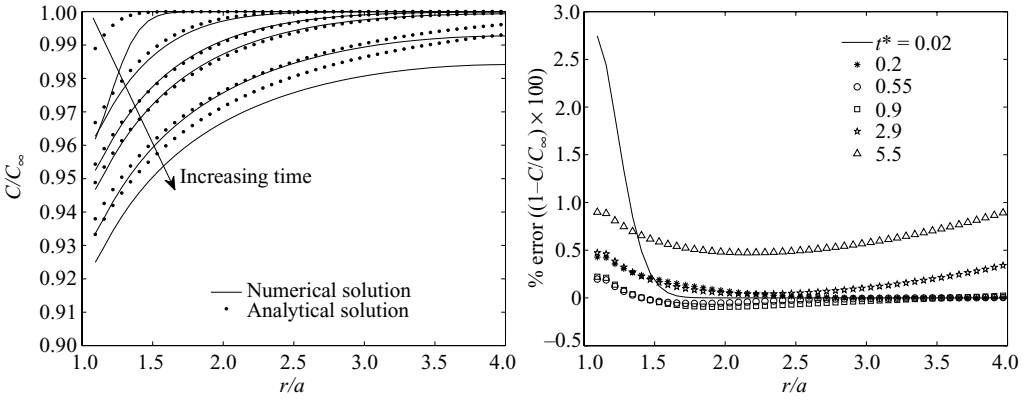

(*a*) Variation of bulk concentration. (*b*) Percentage error in bulk concentration.

FIGURE 19. Variation of bulk concentration as a function of distance from the centre of the particle and the percentage error compared with the analytical results. The analytical result is from Muradoglu & Tryggvason (2008). The six non-dimensional times plotted here correspond to $t^* = 0.02, 0.2, 0.55, 0.9, 2.9$ and 5.5.

the surfactant in the bulk as a function of the distance from the centre, r, of the bubble, for various times. The higher curves correspond to shorter times. Figure 19(*b*) shows the percentage error in the computation of the bulk surfactant concentration for various times. It can be noted from figures 18, 19(*a*) and 19(*b*) that the numerical predictions compare very well with the analytical solution for the grid sizes employed.

A.3. *Marangoni effects*

To test for the Marangoni effect, we consider a bubble that is initially covered with a non-uniformly distributed insoluble surfactant with an interface concentration Γ given by

$$\Gamma = \Gamma_\infty z/L, \tag{A 4}$$

where z is the axial coordinate, Γ_∞ is a reference concentration and L is the length of the tube. The bubble has a radius a and is placed axisymmetrically in the tube of radius $R = 5a$ and length $L = 15a$. Initially, the bubble and the bulk medium are quiescent. The motion of the bubble is therefore solely due to Marangoni stresses. This example is derived from the thermocapillary migration study of a viscous drop by Young, Goldstein & Block (1959). A linear equation of state, relating the surface tension σ with Γ, Γ_∞, the surface tension of the clean interface σ_s and an elasticity number β_s of the form

$$\sigma = \sigma_s \left(1 - \beta_s \frac{\Gamma}{\Gamma_\infty}\right) \tag{A 5}$$

is employed. The steady terminal velocity of the drop is given by Young *et al.* (1959) as

$$V_{YGB} = \frac{2\sigma_s \beta_s a}{L\,(6\mu_0 + 9\mu_d)}. \tag{A 6}$$

With $\rho_0 = \rho_d = 0.2$, $\mu_0 = \mu_d = 0.1$, $a = 0.5$ and $\beta_s = 2.0$, the comparison of the terminal velocity of the drop with the theoretical result is shown in figure 20. This plot shows the velocity approaching the theoretical result ($v/V_{YGB} = 1$). The small difference at the end may be attributed to the bounding wall present in our simulation.

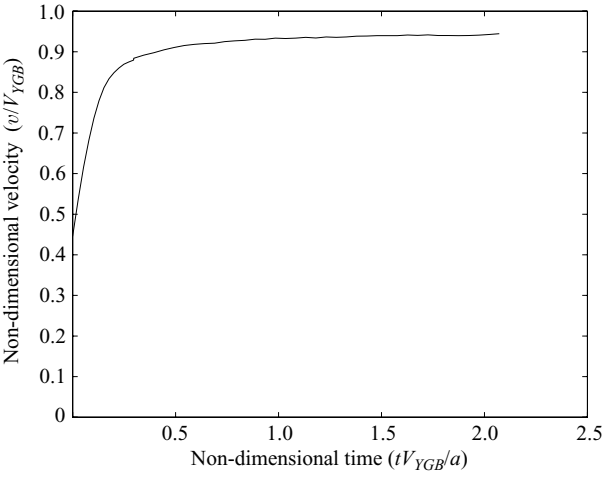

FIGURE 20. Prediction for non-dimensional terminal velocity of a bubble motion purely driven by Maragoni forces.

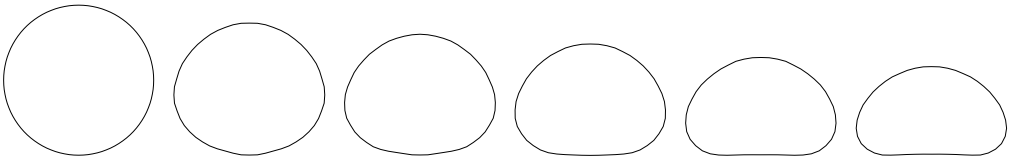

FIGURE 21. Shape of an axisymmetric bubble rising in a tube. The length scale for each of these times is not identical.

A.4. *Buoyancy-driven rising bubble*

The results for an axisymmetric bubble rising in a cylindrical tube, in the presence of a surfactant, due to buoyancy has been computed by Muradoglu & Tryggvason (2008). Here we show a comparison between our computations and their results. The values for the various parameters used in this comparison, derived from figure 21 of Muradoglu & Tryggvason (2008), are $\rho_g/\rho_l = 0.1$, $\mu_g/\mu_l = 0.025$, $Pe = 100$, $Pe_s = 100$, $k_a C_0/k_d = 1$, $\Gamma_\infty/C_0 d = 0.2$, $\Re T\Gamma_\infty/\sigma_s = 0.5$, $\Delta\rho g d/\sigma_s = 10$ and $\Delta\rho g\mu_l^4/\rho_l^2\sigma_s^3 = 0.001$. The tube diameter is $5d$ and the length is $30d$. The bubble is initially clean and spherical. Under these conditions, the contaminated bubble deforms strongly. Bubble shapes for various times are shown in figure 21 and match well with their results.

Appendix B. Casson model

In (2.7), the expressions for μ_∞ and τ_y as functions of core haematocrit H_C are given by Das, Johnson & Popel (2000) as

$$\mu_\infty = \frac{\mu_p}{(1-H_C)^{C_1}} \quad , \quad \tau_y^{1/2} = C_2\left[\left(\frac{1}{1-H_C}\right)^{C_1/2} - 1\right]. \tag{B 1}$$

Here, C_1, C_2 are constants whose values for human blood are given as 2.0 and 0.3315, respectively. The evaluations of the equations require a knowledge of H_C, δ and β. In regard to the haematocrit, the discharge haematocrit H_D is usually a

known quantity (taken as 0.45 here). For $\delta > 0$, the core haematocrit H_C, which is based upon the core volume, is larger than H_D. For a given vessel size, the relationships between H_D, H_C, δ and β are nonlinear. For vessels of diameter in the range $20\,\mu\text{m} \leqslant d \leqslant 300\,\mu\text{m}$, Sharan & Popel (2001) have described methods that are based on nonlinear coupled differential equations supplemented by experimental data. These methods establish relationships between H_D, H_C, δ and β for known values of d and H_D. We have previously solved these equations for $d = 40\,\mu\text{m}$ (small arteriole) and $100\,\mu\text{m}$ (large arteriole) for $H_D = 0.45$ (Mukundakrishnan *et al.* 2008*a*) and have documented values for H_C, δ and β. In Mukundakrishnan *et al.* (2008*a*), we have also examined a vessel size $d = 2000\,\mu\text{m}$ (small artery). At such a large radius, $\delta \to 0$ and $H_C \sim H_D$.

REFERENCES

Ayyaswamy, P. S. 2008 Introduction to biofluid mechanics. In *Fluid Mechanics*, 4th ed. (ed. P. K. Kundu & Ira M. Cohen), pp. 765–840. Academic Press.

Batchelor, G. K. 1967 *An Introduction to Fluid Mechanics*. Cambridge University Press.

Berger, S. A., Goldsmith, W. & Lewis, E. R. 1996 *Introduction to Bioengineering*. Oxford University Press.

Bond, W. N. & Newton, D. A. 1928 Bubbles, drops and stokes' law (paper 2). *Phil. Mag.* **5**, 794–800.

Branger, A. B. & Eckmann, D. M. 1999 Theoretical and experimental intravascular gas embolism absorption dynamics. *J. Appl. Physiol.* **87**, 1287–1295.

Branger, A. B. & Eckmann, D. M. 2002 Accelerated arteriolar gas embolism reabsorption by an exogenous surfactant. *Anesthesiology* **96** (4), 971–979.

Butler, P. J., Tsou, T. C., Li, J. Y. S., Usami, S. & Chien, S. 2001 Rate sensitivity of shear-induced changes in the lateral diffusion of endothelial cell membrane lipids: a role for membrane perturbation in shear-induced mapk activation. *Faseb J.* **15**, 216–218.

Cavanagh, D. P. & Eckmann, D. M. 1999 Interfacial dynamics of stationary gas bubbles in flows in inclined tubes. *J. Fluid Mech.* **398**, 225–244.

Chang, C.-H. & Franses, E. I. 1995 Adsorption dynamics of surfactants at the air/water interface: a critical review of mathematical models, data, and mechanisms. *Colloids Surfaces A: Physicochem. Engng Aspects* **100**, 1–45.

Colella, P. 1990 A multidimensional second order Godunov scheme for conservation laws. *J. Comput. Phys.* **87**, 171.

Das, B., Johnson, P. C. & Popel, A. S. 2000 Computational fluid dynamic studies of leukocyte adhesion effects on non-Newtonian blood flow through microvessels. *Biorheology* **37** (3), 239–258.

Eckmann, D. M. & Armstead, S. C. B. S. 2006 Influence of endothelial glycocalyx degradation and surfactants on air embolism adhesion. *Anesthesiology* **105** (6), 1220–1227.

Eckmann, D. M., Kobayashi, S. & Li, M. 2005 Microvascular embolization following polidocanol microfoam sclerosant administration. *Dermatologic Surgery* **31** (5), 636–643.

Eckmann, D. M. & Lomivorotov, V. N. 2003 Microvascular gas embolization clearance following perfluorocarbon administration. *J. Appl. Physiol.* **94**, 860–868.

Eckmann, D. M., Zhang, J., Lampe, J. & Ayyaswamy, P. S. 2006 Gas embolism and surfactant-based intervention. *Ann. New York Acad. Sci.* **1077**, 256–269.

Eggleton, C. D., Pawar, Y. P. & Stebe, K. J. 1999 Insoluble surfactant on a drop in an extension flow: a generalization of the stagnated surface limit to deformable interfaces. *J. Fluid Mech.* **385**, 79–99.

Eggleton, C. D., Tsai, T. M. & Stebe, K. J. 2001 Tip streaming from a drop in the presence of surfactants. *Phys. Rev. Lett.* **87** (4), 048302(1–4).

Fung, Y. C. 1997 *Biomechanics: Circulation*. Springer.

Ghadiali, S. N. & Gaver, D. P. 2003 The influence of non-equilibrium surfactant dynamics on the flow of a semi-infinite bubble in a rigid cylindrical capillary tube. *J. Fluid Mech.* **478**, 165–196.

Griffith, B. E. & Peskin, C. S. 2005 On the order of accuracy of the immersed boundary method: higher-order convergence rates for sufficiently smooth problems. *J. Comput. Phys.* **208**, 75–105.

Happel, J. & Brenner, H. 1983 *Low Reynolds Number Hydrodynamics*. Martinus Nijhoff.

Huang, H. D., Kamm, R. D. & Lee, R. T. 2004 Cell mechanics and mechanotransduction: pathways, probes, and physiology. *Am. J. Physiol. Cell Physiol.* **287**, C1–C11.

Jacqmin, D. 1999 Calculation of two-phase Navier–Stokes flows using phase-field modelling. *J. Comput. Phys.* **55**, 96.

James, A. J. & Lowengrub, J. 2004 A surfactant-conserving volume-of-fluid method for interfacial flows within soluble surfactant. *J. Comput. Phys.* **201**, 685–722.

Johnson, R. A. & Borhan, A. 2003 Pressure-driven motion of surfactant-laden drops through cylindrical capillaries: effect of surfactant solubility. *J. Colloid Interface Sci.* **261**, 529–541.

Johnson, R. E. & Sadhal, S. S. 1983 Stokes flow past bubbles and drops partially coated with thin films. Part 2. Thin films with internal circulation – a perturbation solution. *J. Fluid Mech.* **132**, 295–318.

Lee, L. & Leveque, R. 2003 An immersed interface method for incompressible Navier–Stokes equations. *SIAM J. Sci. Comput.* **25**, 832.

Levich, V. G. 1962 *Physicochemical Hydrodynamics*. Prentice Hall.

Li, X. F. & Pozrikidis, C. 1997 The effect of surfactant on drop deformation and on the rheology of dilute emulsion in stokes flow. *J. Fluid Mech.* **341**, 165–194.

Liu, S. Q., Ruan, Y. Y., Tang, D., Li, Y. C., Goldman, J. & Zhong, L. 2002 A possible role of initial cell death due to mechanical stretch in the regulation of subsequent cell proliferation in experimental vein grafts. *Biomech. Model. Mechanobiol.* **1** (1), 17–27.

McKinney, J. S., Willoughby, K. A., Liang, S. & Ellis, E. F. 1996 Stretch-induced injury of cultured neuronal, glial, and endothelial cells: effect of polyethylene glycol-conjugated superoxide dismutase. *Stroke* **27** (5), 934–940.

McNeil, P. L. & Steinhardt, R. A. 1997 Loss, restoration, and maintenance of plasma membrane integrity. *J. Cell Biol.* **137**, 1–4.

Mendez, J. L., Rickman, O. B. & Hubmayr, R. D. 2004 Plasma membrane stress failure in ventilator-injured lungs – a hypothesis about osmoregulation and the pharmacologic protection of the lungs against deformation. *Biol. Neonate* **85**, 290–292.

Milliken, W. J. & Leal, L. G. 1994 The influence of surfactant on the deformation and breakup of a viscous drop. *J. Colloid Interface Sci.* **166**, 275–285.

Mukundakrishnan, K., Ayyaswamy, P. S. & Eckmann, D. M. 2008*a* Finite-sized gas bubble motion in a blood vessel: non-newtonian effects. *Phys. Rev.* E **78**, 036303(1–15).

Mukundakrishnan, K., Ayyaswamy, P. S. & Eckmann, D. M. 2009 Bubble motion in a blood vessel: shear stress induced endothelial cell injury. *J. Biomech. Engng* **131** (7), 074516.

Mukundakrishnan, K., Eckmann, D. M. & Ayyaswamy, P. S. 2008*b* Bubble motion through a generalized power-law fluid flowing in a vertical tube. *Ann. New York Acad. Sci.* **1161**, 256–267.

Mukundakrishnan, K., Quan, S., Eckmann, D. M. & Ayyaswamy, P. S. 2007 Numerical study of wall effects on buoyant gas-bubble rise in a liquid-filled finite cylinder. *Phys. Rev.* E **76**, 036308(1–15).

Muradoglu, M. & Tryggvason, G. 2008 A front-tracking method for computation of interfacial flows with soluble surfactants. *J. Comput. Phys.* **227**, 2238–2262.

Oguz, H. N. & Sadhal, S. S. 1988 Effects of soluble and insoluble surfactants on the motion of drops. *J. Fluid Mech.* **194**, 563–579.

Oike, M., Droogmans, G. & Nilius, B. 1994 Mechanosensitive Ca2+ transients in endothelial cells from human umbilical vein. *Proc. Natl Acad. Sci. USA* **91** (8), 2940–2944.

Osher, S. & Fedkiw, R. 2001 Level set methods: an overview and some recent results. *J. Comput. Phys.* **169**, 463.

Palaparthi, R., Papageorgiou, D. T. & Maldarelli, C. 2006 Theory and experiments on the stagnant cap regime in the motion of spherical surfactant-laden bubbles. *J. Fluid Mech.* **559**, 1–44.

Papanastasiou, T. C. 1987 Flows of materials with yield. *J. Rheol.* **31** (5), 385–404.

Park, C. W. 1992 Influence of soluble surfactant on the motion of a finite bubble in a capillary tube. *Phys. Fluids* A **4** (11), 2335–2347.

Quan, S. & Schmidt, D. P. 2007 A moving mesh interface tracking method for 3d incompressible two-phase flows. *J. Comput. Phys.* **221**, 761–780.

Radl, S., Tryggvason, G. & Khinast, J. G. 2007 Flow and mass transfer of fully resolved bubbles in non-Newtonian fluids. *AIChE J.* **53**, 1861–1878.

Rodrigue, D., De Kee, D. & Chan Man Fong, C. F. 1996 An experimental study of the effect of surfactants on the free rise velocity of gas bubbles. *J. Non-Newt. Fluid Mech.* **66** (3), 213–232.

Rodrigue, D., De Kee, D., Chan Man Fong, C. F. & Yao, J. 1999 The slow motion of a single gas bubble in a non-newtonian fluid containing surfactants. *J. Non-Newt. Fluid Mech.* **86**, 211–227.

Sadhal, S. S., Ayyaswamy, P. S. & Chung, J. N. 1997 *Transport Phenomena with Drops and Bubbles*. Springer.

Sadhal, S. S. & Johnson, R. E. 1983 Stokes flow past bubbles and drops partially coated with thin films. Part 1. Stagnant cap of surfactant film - exact solution. *J. Fluid Mech.* **133**, 65–81.

Scardovelli, R. & Zaleski, S. 1999 Direct numerical simulation of free surface and interfacial flow. *Ann. Rev. Fluid Mech.* **31**, 576.

Sharan, M. & Popel, A. S. 2001 A two-phase model for blood flow in narrow tubes with increased viscosity near the wall. *Biorheology* **38**, 415–428.

Shin, S., Abdel-Khalik, S. I., Daru, V. & Juric, D. 2005 Accurate representation of surface tension using the level contour reconstruction method. *J. Comput. Phys.* **203**, 493–516.

Shin, S. & Juric, D. 2002 Modelling three-dimensional multiphase flow using a level contour reconstruction method for front tracking without connectivity. *J. Comput. Phys.* **180**, 427–470.

Sigurdson, W. J., Sachs, F. & Diamond, S. L. 1993 Mechanical perturbation of cultured human endothelial cells causes rapid increases of intracellular calcium. *Am. J. Physiol. Heart Circ. Physiol.* **264** (6), H1745–H1752.

Somasundaran, P. 2006 *Encyclopedia of Surface and Colloid Science*. CRC Press.

Stone, H. A. 1990 A simple derivation of the time-dependent convective-diffusive equation for surfactant transport along a deforming interface. *Phys. Fluids* A **2**, 111–112.

Sussman, M., Almgren, A. S., Bell, J. B., Colella, P., Howell, L. & Welcome, M. 1999 An adaptive level set approach for incompressible two-phase flows. *J. Comput. Phys.* **148**, 81.

Sussman, M. & Puckett, E. G. 2000 A coupled level set and volume-of-fluid method for computing 3D and axisymmetric incompressible two-phase flows. *J. Comput. Phys.* **162** (2), 301–337.

Suzuki, A., Armstead, S. C. & Eckmann, D. M. 2004 Surfactant reduction in embolism bubble adhesion and endothelial damage. *Anesthesiology* **101**, 97–103.

Swaminathan, T. N., Ayyaswamy, P. S. & Eckmann, D. M. 2009 Favourable conditions for exogenous surfactant-based intervention of gas embolism (in preparation).

Torres, D. J. & Brackbill, J. U. 2000 The point-set method: front tracking without connectivity. *J. Comput. Phys.* **165**, 620.

Tryggvason, G., Bunner, B., Esmaeeli, A., Juric, D., Al-Rawahi, N., Tauber, W., Han, J., Nas, S. & Jan, Y. J. 2001 A front-tracking method for the computations of multiphase flow. *J. Comput. Phys.* **169**, 708–759.

Tsai, T. M. & Miksis, M. J. 1994 Dynamics of a drop in a constricted capillary tube. *J. Fluid Mech.* **274**, 197–217.

Udaykumar, H. S., Tran, L., Belk, D. M. & Vanden, K. J. 2003 An Eulerian method for computation of multimaterial impact with ENO shock-capturing and sharp interfaces. *J. Comput. Phys.* **186**, 136–177.

Unverdi, S. O. & Tryggvason, G. 1992 A front-tracking method for viscous incompressible, multi-fluid flows. *J. Comput. Phys.* **100** (1), 25–37.

Van Sint Annaland, M., Dijkhuizen, W., Deen, N. G. & Kuipers, J. A. M. 2006 Numerical simulation of gas bubbles behaviour using a 3D front tracking method. *AIChE J.* **52**, 99–110.

Vlahakis, N. E. & Hubmayr, R. D. 2000 Invited review: plasma membrane stress failure in alveolar epithelial cells. *J. Appl. Physiol.* **89**, 2490–2496.

Wesseling, P. 1992 *An Introduction to Multigrid Methods*. John Wiley & Sons.

Yon, S. & Pozrikidis, C. 1998 A finite volume/boundary-element method for flow past interfaces in the presence of surfactants, with application to shear flow past a viscous drop. *Comput. Fluids* **27**, 879–902.

Young, N. O., Goldstein, J. S. & Block, M. J. 1959 The motion of bubbles in a vertical temperature gradient. *J. Fluid Mech.* **6**, 350.

Zhang, J., Eckmann, D. M. & Ayyaswamy, P. S. 2006 A front tracking method for a deformable intravascular bubble in a tube with soluble surfactant transport. *J. Comput. Phys.* **214**, 366–396.